Materials Advances

ROYAL SOCIETY OF CHEMISTRY

PAPER

View Article Online
View Journal | View Issue



Check for updates

Cite this: *Mater. Adv.*, 2025, 6, 5758

# Thermally stable $Li^+$ co-doped $ZnMoO_4:Eu^{3+}$ phosphors for white LEDs, nitroaromatic sensing and low temperature non-contact optical thermometry applications†

Astha Tyagi, [a] M. Rakshita, [b] D. Haranath [b] and Chikkadasappa Shivakumara *[a]

Received 28th March 2025,
Accepted 30th June 2025

DOI: 10.1039/d5ma00280j

rsc.li/materials-advances

The development of multifunctional luminescent materials with high thermal stability and sensitivity is crucial for advanced lighting, chemical sensing, and temperature monitoring applications. However, many existing red-emitting phosphors are limited by poor thermal stability, weak chemical selectivity, and narrow functional temperature windows. In this work, we present a $Li^+$ co-doped $ZnMoO_4:Eu^{3+}$ phosphor ($Zn_{0.88}Eu_{0.09}Li_{0.03}MoO_4$, ZELMO) that overcomes these limitations through $Li^+$ incorporation, which enhances crystallinity, facilitates charge compensation, and modifies the local crystal field around $Eu^{3+}$ ions. ZELMO exhibits a two-fold increase in photoluminescence intensity, excellent color purity (93.6%), and thermal stability with 83% intensity retention at 423 K. It also demonstrates selective and ultra-sensitive detection of 4-nitrophenol, with a low detection limit of 12 nM. Moreover, ZELMO enables non-contact optical thermometry in the 15–295 K range, achieving a maximum relative sensitivity of 0.61% $K^{-1}$. These results position ZELMO as a promising red-emitting phosphor for multifunctional use in solid-state lighting, environmental sensing, and low-temperature optical thermometry.

## 1. Introduction

The development of advanced luminescent materials has become essential for diverse applications, such as bio-imaging,[1] temperature sensing,[2] optical heating,[3] display technologies,[4] chemical sensing,[5] solid-state lighting,[6] and white light emission sources.[7] Phosphor-based white light-emitting diodes (WLEDs) play a significant role due to their widespread use in general illumination and as backlights for liquid crystal displays (LCDs).[8] Commercial WLEDs typically employ $Ce^{3+}$-activated garnet yellow phosphors coated on blue-emitting LED chips.[9–12] However, the lack of a red-emitting component in these systems often leads to a reduced color rendering index (CRI $<$ 75) and higher correlated color temperature (CCT $>$ 4500 K), adversely affecting the overall color quality.[13,14] To overcome this limitation, the inclusion of red-emitting phosphors, especially $Eu^{3+}$-activated oxide phosphors, has shown significant effectiveness. These materials are recognized for their narrow emission bands, excellent color purity, and remarkable quantum efficiency, making them ideal candidates for enhancing WLED performance.[15–17]

Beyond lighting applications, the selective detection of nitroaromatic compounds has gained considerable attention due to their widespread use in explosives, industrial processes, and agriculture, as well as their potential environmental and health hazards.[18,19] Exposure to 4-NP (*para*-nitrophenol) can result in critical health complications, including methemoglobinemia, damage to the kidneys and liver, persistent headaches, and nausea.[20,21] Due to its toxicity and potential carcinogenicity, the U.S. Environmental Protection Agency has designated 4-NP as a "Priority Pollutant".[22] These factors highlight the urgent need for highly sensitive and selective detection

[a] *Solid State and Structural Chemistry Unit, Indian Institute of Science, Bangalore-560012, India. E-mail: asthatyagi@iisc.ac.in, shiva@iisc.ac.in*

[b] *Luminescent Materials and Devices (LMD) Group, Department of Physics, National Institute of Technology, Warangal, 506004, Telangana, India. E-mail: rakshitaammulu1997@gmail.com, haranath@nitw.ac.in*

† Electronic supplementary information (ESI) available: Additional structural and optical characterization data to complement the main text. Fig. S1 shows the powder XRD patterns of $Zn_{(0.91-y)}Eu_{0.09}Li_yMoO_4$ phosphors with different lithium concentrations ($y$ = 0.01, 0.03, and 0.05). Fig. S2 presents the CIE chromaticity diagram of the $ZnMoO_4$ host material. Fig. S3 shows the PL decay curve of ZELMO with and without 4-NP. Table S1 lists the Rietveld refined structural parameters of $ZnMoO_4$. Table S2 summarizes the CIE 1931 chromaticity coordinates, correlated color temperature (CCT), and color purity values of $ZnMoO_4:Eu^{3+},Li^+$ phosphors under 394 nm excitation. Table S3 provides detailed Judd–Ofelt analysis, including intensity parameters ($\Omega_2$ and $\Omega_4$), radiative transition probabilities, radiative lifetimes, branching ratios, and asymmetric ratios. Lastly, Table S4 contains the quantitative evaluation of optical properties such as effective bandwidth, stimulated emission cross-section, gain bandwidth, and optical gain for the $ZnMoO_4:Eu^{3+},Li^+$ phosphors. Table S5 shows comparative evaluation of the stimulated emission cross-sections ($\sigma_e$) corresponding to the transitions of $Eu^{3+}$ ions in different host matrices. See DOI: https://doi.org/10.1039/d5ma00280j

methods. Luminescent materials, such as $Eu^{3+}$-doped phosphors, offer a promising approach for addressing this challenge, enabling efficient and accurate detection of 4-NP.[23]

Accurate and efficient temperature sensing at low temperatures is essential for a wide range of disciplines, including fundamental sciences, engineering, manufacturing, metallurgy, and aerospace.[24,25] Traditional temperature sensors, such as platinum resistance temperature detectors (RTDs),[26] specialized thermistors,[27] and silicon diodes,[28] have been widely used due to their sensitivity and reliability. However, these sensors are typically large, require physical contact with the object being measured, and are unsuitable for remote temperature detection in large-area thermal distributions, fast-moving objects, or micro- and nanoscale systems.[29] In contrast, luminescence-based ratiometric techniques offer a promising alternative for precise and efficient temperature measurements. These methods are non-invasive, self-calibrating, and provide high spatial resolution and sensitivity.[30,31] Utilizing the temperature-dependent photoluminescence of rare-earth-doped materials, such as $Eu^{3+}$-activated phosphors, this technique enables innovative, accurate, and scalable approaches to remote temperature sensing.[32]

Among potential host materials, $ZnMoO_4$ stands out due to its excellent chemical stability,[33] wide band gap,[34] and highly tunable photoluminescence properties.[35] These attributes, combined with its ability to accommodate rare-earth dopants like $Eu^{3+}$, make $ZnMoO_4$ a promising candidate for developing high-performance red phosphors.

In this study, we explore the optimization of $Li^+$ co-doped $ZnMoO_4$:$Eu^{3+}$ for multiple applications, including its use as a red component in white LEDs, as well as for selective sensing of nitroaromatic compounds and temperature sensing. By systematically varying Eu concentration and co-doping with lithium, we identify the optimal dopant levels to enhance the photoluminescent properties. The material shows excellent sensitivity and selectivity for detecting nitroaromatic compounds, particularly *para*-nitrophenol, and demonstrates thermal stability at high temperatures, making it suitable for demanding applications. Additionally, temperature-dependent PL studies highlight its potential for temperature sensing. This work emphasizes the multifunctional potential of Eu-doped $ZnMoO_4$ as a versatile material for optoelectronic devices, lighting technologies, and sensing applications.

# 2. Experiments

## 2.1. Materials and methods

The phosphors with compositions $Zn_{(1-x)}Eu_xMoO_4$ ($0 \leq x \leq 0.11$) and $Zn_{(0.91-y)}Eu_{0.09}Li_yMoO_4$ ($0 \leq y \leq 0.05$) were synthesized using the nitrate–citrate gel combustion method, a process well-suited for achieving homogeneous and fine powders. $Zn(NO_3)_2{\cdot}6H_2O$ (99%, SD fine Chemicals), $(NH_4)_6Mo_7O_{24}{\cdot}4H_2O$ (99%, SD fine Chemicals), $Eu_2O_3$ (99.9%, Sigma-Aldrich), and $Li_2CO_3$ (99%, Loba Chemie) were used as precursors, and citric acid (99.5%, Spectrochem) was used as a fuel for auto combustion. $Zn(NO_3)_2{\cdot}6H_2O$ and $(NH_4)_6Mo_7O_{24}{\cdot}4H_2O$ were dissolved in deionized water, while $Eu_2O_3$ and $Li_2CO_3$ were dissolved in dilute nitric acid (1 : 1, v/v). After combining the solutions, citric acid was added as a fuel. Heating at 150 °C resulted in gel formation, which combusted at ~200 °C to yield powders. These were calcined at 700 °C for 3 hours to produce phase-pure phosphors.

To perform the screening for nitroaromatic compounds, 50 mM solutions of various nitroaromatics were prepared in a pH 7 buffer solution (Merck, ETS). The synthesized $Zn_{0.88}Eu_{0.09}Li_{0.03}MoO_4$ phosphor was added at a concentration of 1 mg $mL^{-1}$ to these solutions followed by 30 minutes of sonication to ensure uniformity prior to measurements. Similarly, for *para*-nitrophenol (4-NP) detection, the phosphor was mixed with PNP solutions (1 nM to 200 μM) prepared in the same pH 7 buffer, with sonication for 30 minutes. This preparation ensures reproducibility and highlights the selective sensing capability of the phosphor.

The $Zn_{0.88}Eu_{0.09}Li_{0.03}MoO_4$-polyvinyl alcohol (PVA) film was prepared by mixing a sonicated phosphor solution (0.2 g in deionized water) with a PVA solution (2 g in 50 mL deionized water), heating at 90 °C under stirring. The mixture was subsequently transferred onto a glass substrate and dried for 24 hours.

## 2.2. Characterization

Powder X-ray diffraction (XRD) analysis of the samples was performed using a PANalytical Empyrean diffractometer, operating at 45 kV and 30 mA with Cu Kα radiation ($\lambda$ = 1.5418 Å). Data was acquired over a $2\theta$ range of 10° to 80° with a scan rate of 2° $min^{-1}$. Rietveld refinement was carried out using Fullprof Suite-2000 software to determine the structural parameters from the XRD patterns. X-ray photoelectron spectroscopy (XPS) study was conducted using a Thermo Scientific K-Alpha surface analysis instrument. The direct excitation $^7Li$ magic angle spinning (MAS) experiments were conducted at room temperature using a 9.4 T solid-state NMR spectrometer ($^7Li$ Larmor frequency of 155.452 MHz) with a MAS frequency of 10 kHz. Fourier transform infrared (FTIR) spectroscopy was performed to analyze the functional groups present in the sample. The measurements were conducted in the range of 350–4000 $cm^{-1}$ using a PerkinElmer Frontier spectrometer in attenuated total reflectance (ATR) mode. Diffuse reflectance spectra (DRS) were acquired using a PerkinElmer Lambda 750 spectrometer to evaluate the band gap of the compounds. Photoluminescence (PL) emission and excitation measurements were performed using a Jobin-Yvon FluoroMax spectrometer, which was equipped with a 450 W xenon lamp serving as the excitation source. The temperature-dependent PL studies in the range of 303 K to 573 K were conducted using a Horiba Scientific spectrofluorometer (model: Fluorolog-3). The temperature-dependent PL studies in the range of 15 K to 295 K were conducted using the WITec Alpha 300R photoluminescence Raman microscope and spectrometer. For lifetime measurements, the Edinburgh PL instrument was used with a microsecond flash lamp. Photoluminescence quantum yield (QY) measurements were carried out using an Edinburgh

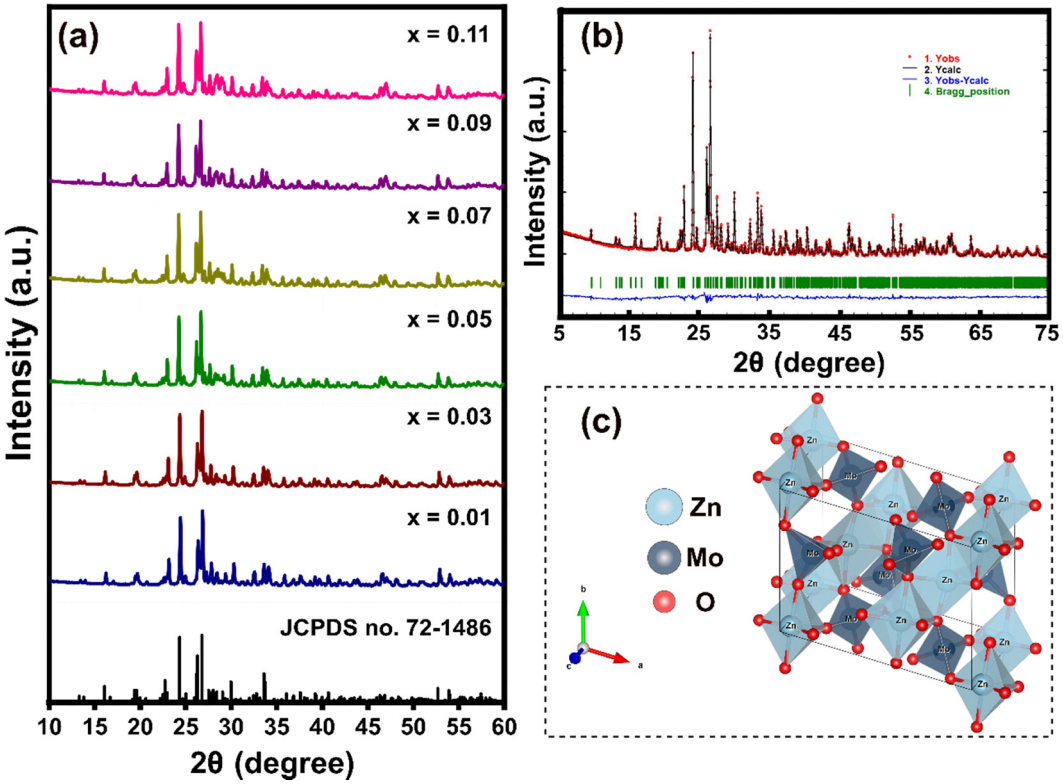


Fig. 1 (a) XRD patterns of $Zn_{(1-x)}Eu_xMoO_4$ ($0.01 \leq x \leq 0.11$) phosphors. (b) Observed, calculated, and difference XRD patterns of $ZnMoO_4$. (c) Crystal structure of $ZnMoO_4$.

Instruments FLS1000 photoluminescence spectrometer equipped with a 450 W xenon arc lamp and an integrating sphere (model N-M01) for absolute measurements. The measurements were carried out at room temperature with an excitation wavelength of 394 nm. A $BaSO_4$ coated reference was employed to obtain the baseline spectrum necessary for accurate QY calculation. The QY was calculated using the software provided by the instrument, following standard protocols.

## 3. Results and discussion

### 3.1. Structural analysis

The X-ray diffraction (XRD) patterns of the synthesized compounds were analysed to study the crystal structure and the influence of dopants on the crystal lattice. The XRD patterns of the $Zn_{1-x}Eu_xMoO_4$ ($0.01 \leq x \leq 0.11$) phosphors are shown in Fig. 1(a). The diffraction peaks of all the synthesized compounds closely aligned with those in the JCPDS file no. 72-1486,[36] with no evidence of secondary phases or impurities from the starting materials, indicating the formation of single-phase compounds. Additionally, it was observed that the low concentration of $Eu^{3+}$ did not significantly influence the host lattice by replacing $Zn^{2+}$ sites. This was confirmed by calculating the percentage difference in radii ($R_r$) using the following expression:[37]

$$R_r = \frac{R_h(CN) - R_d(CN)}{R_d(CN)} \times 100\% \quad (1)$$

For a coordination number (CN) of 6, the radius of $Zn^{2+}$ ions ($R_h$(CN)) is 0.74 Å, while that of $Eu^{3+}$ doping ions ($R_d$(CN)) is 0.94 Å. The calculated percentage difference in radii ($R_r$) is approximately 27% for CN = 6, suggesting that $Eu^{3+}$ ions can effectively substitute $Zn^{2+}$ sites, as the percentage difference remains below 30%.

Rietveld refinement analysis was conducted to determine the structural parameters of the host material using powder XRD data. The results confirmed that the synthesized compound crystallized in a triclinic structure with the space group $P\bar{1}$ (no. 2). Fig. 1(b) illustrates the observed, calculated, and difference powder XRD patterns for the $ZnMoO_4$ compound, showing excellent agreement between the observed and calculated data. The refined structural parameters for the sample are presented in Table S1 (ESI†). Furthermore, the VESTA program was employed to model the crystal structure of the $ZnMoO_4$ host, utilizing atomic coordination and lattice parameters, as depicted in Fig. 1(c). It shows that the crystal structure of $ZnMoO_4$ consists of a series of distorted Mo–O tetrahedra, Zn–O octahedra, and Zn–O pentahedra. The $Eu^{3+}$ ions replaced the $Zn^{2+}$ sites in the $ZnMoO_4$ system.

Fig. S1 (ESI†) presents the XRD patterns of $Li^+$-co-doped $Zn_{0.91}Eu_{0.09}MoO_4$ phosphors. The patterns align well with those of the $Zn_{0.91}Eu_{0.09}MoO_4$ compound, confirming the retention of the triclinic crystal structure. No impurity peaks were observed for $Li^+$ doping levels up to 5 mol%, indicating the successful incorporation of $Li^+$ ions into the $ZnMoO_4$ lattice.

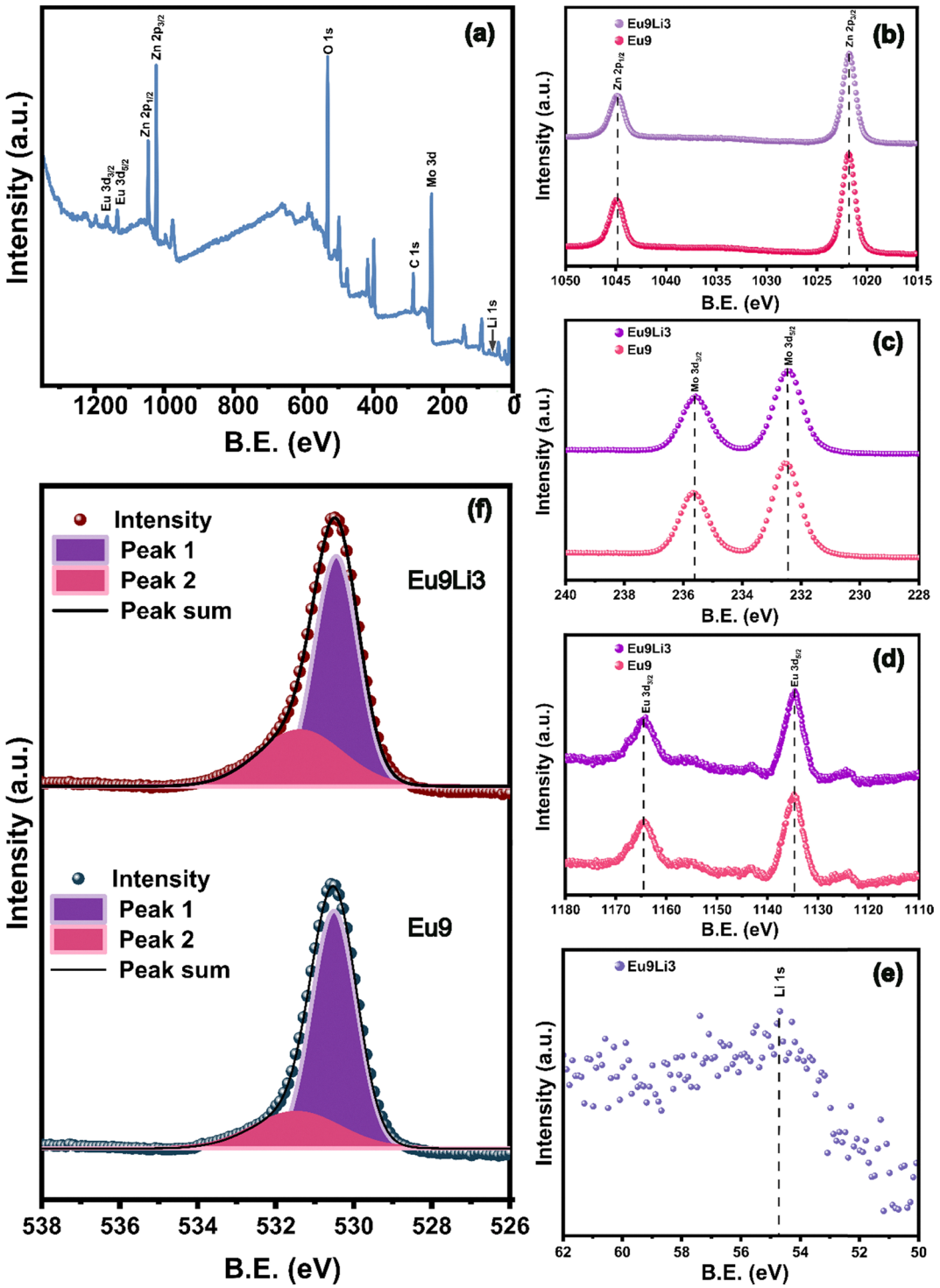


Fig. 2 (a) XPS spectrum of the $Zn_{0.88}Eu_{0.09}Li_{0.03}MoO_4$ phosphor. High resolution XPS spectra of (b) Zn 2p, (c) Mo 3d, (d) Eu 3d, (e) Li 1s, and (f) O 1s.

### 3.2. XPS study

X-ray photoelectron spectroscopy (XPS) analysis was employed to provide in-depth insights into the surface chemical composition and electronic states of the synthesized samples $Zn_{0.91}Eu_{0.09}MoO_4$ and $Zn_{0.88}Eu_{0.09}Li_{0.03}MoO_4$. The binding energy for each element was calibrated using the adventitious carbon peak at 284.8 eV as a reference for correcting any potential charge-induced shifts during the measurements.[38]

Fig. 2(a) shows a survey scan of the $Zn_{0.88}Eu_{0.09}Li_{0.03}MoO_4$ phosphor, with characteristic peaks corresponding to Zn, Mo, O, Eu, and Li, confirming the successful incorporation of these elements into the $ZnMoO_4$ matrix. Importantly, no impurities were detected in the XPS survey scan apart from the

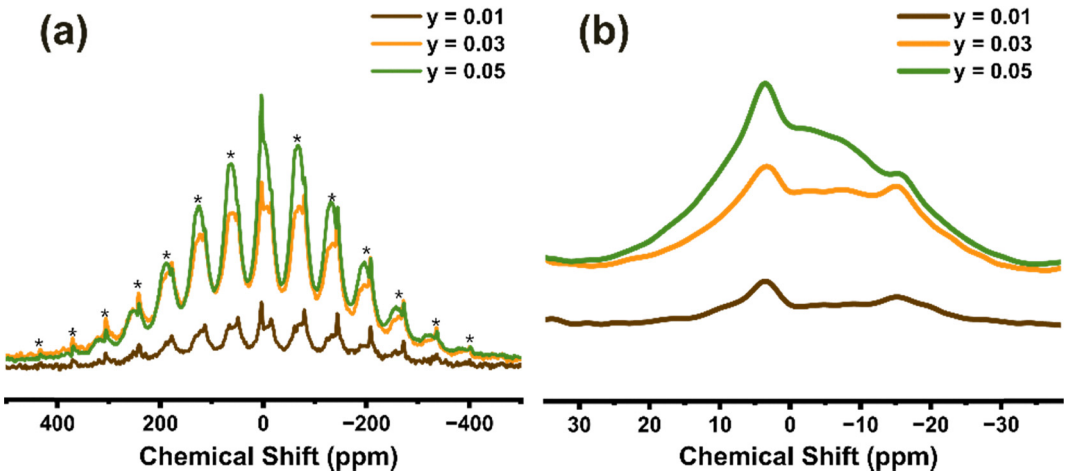


Fig. 3 (a) $^{7}$Li NMR spectra of $Zn_{0.91-y}Eu_{0.09}Li_yMoO_4$ ($y$ = 0.01, 0.03, and 0.05). (b) Magnified view of the isotropic peak for detailed observation.

adventitious carbon peak, indicating the high purity of the synthesized phosphor materials. All the peaks in the survey scan were identified and assigned with reference to the National Institute of Standard Technology (NIST) XPS database.[39] The XPS binding energy spectra of Zn(2p), Mo(3d), Eu(3d), Li(1s), and O(1s) for $Zn_{0.91}Eu_{0.09}MoO_4$ and $Zn_{0.88}Eu_{0.09}Li_{0.03}MoO_4$ samples

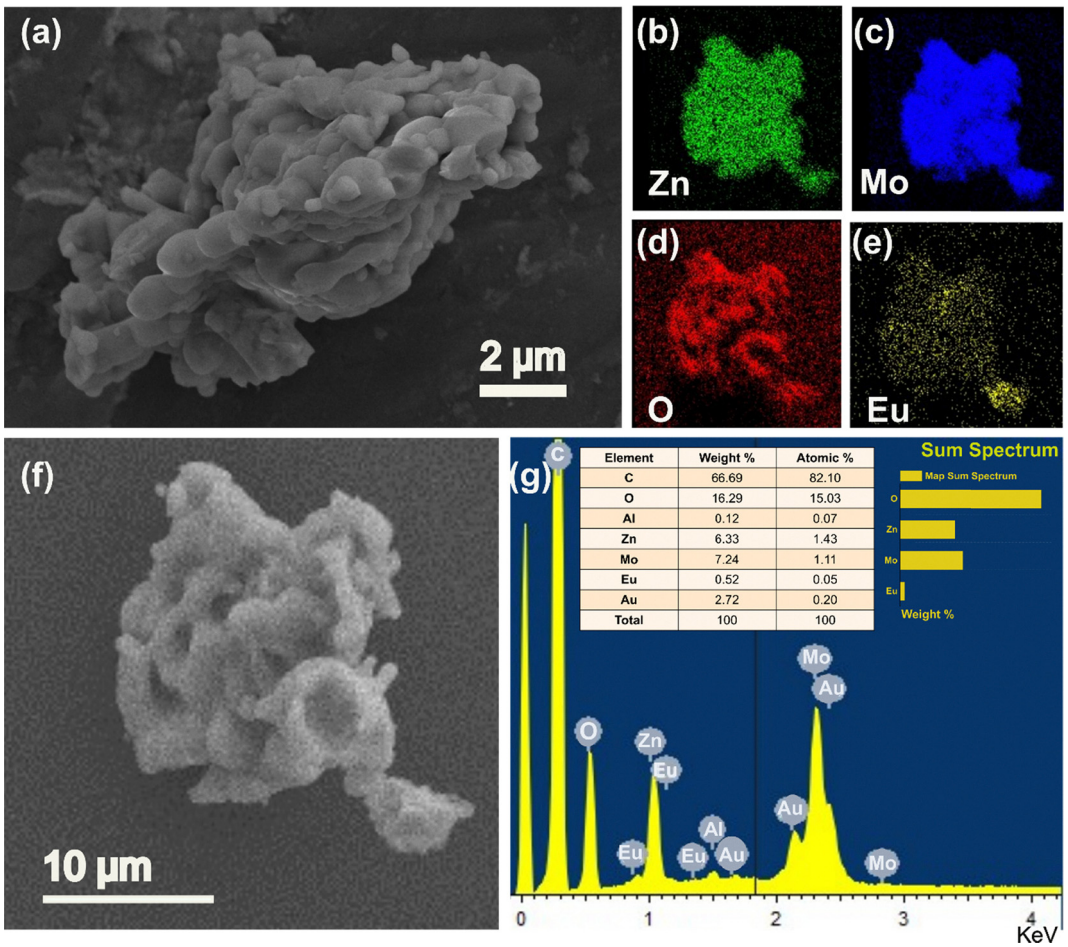


Fig. 4 (a) FESEM image of $Zn_{0.88}Eu_{0.09}Li_{0.03}MoO_4$, elemental mapping images of (b) Zn, (c) Mo, (d) O, and (e) Eu. (f) and (g) EDS image, and spectrum (inset shows atomic% ratio) of $Zn_{0.88}Eu_{0.09}Li_{0.03}MoO_4$.

are shown in Fig. 2(b)–(f). In Fig. 2(b), the Zn $2p_{3/2}$ peak was detected at approximately 1022.0 eV, and the Zn $2p_{1/2}$ peak at around 1045.0 eV, consistent with $Zn^{2+}$ in the $ZnMoO_4$ matrix. These binding energies indicate that zinc remains in the +2 oxidation state in both samples. The presence of both spin–orbit split peaks confirms the stable chemical environment of $Zn^{2+}$ across the samples, highlighting that Li co-doping has a negligible impact on the zinc oxidation state.[40] In Fig. 2(c), the Mo $3d_{5/2}$ and Mo $3d_{3/2}$ peaks appeared around 232.4 eV and 235.6 eV, respectively, corresponding to $Mo^{6+}$ states.[40] In Fig. 2(d), both the Eu $3d_{5/2}$ and Eu $3d_{3/2}$ peaks were observed, confirming the presence of $Eu^{3+}$ in the samples. The Eu $3d_{5/2}$ peak appeared at approximately 1134.5 eV, and the Eu $3d_{3/2}$ peak at around 1164.5 eV.[41] The Li 1s peak (Fig. 2(e)) at 54.7 eV confirmed the successful incorporation of Li into the lattice.[42] The O 1s spectra (Fig. 2(f)) were deconvoluted into two peaks to analyze the oxygen species; peak 1 (purple color) corresponds to lattice oxygen, and peak 2 (pink color) corresponds to oxygen vacancies. The peaks corresponding to lattice oxygen are observed at lower binding energy, while those corresponding to oxygen vacancies are at higher binding energy values. In the case of $Zn_{0.91}Eu_{0.09}MoO_4$, the peaks were detected at around 530.48 eV and 531.71 eV, and in the case of the $Zn_{0.88}Eu_{0.09}Li_{0.03}MoO_4$ phosphor, the peaks were detected at around 530.49 eV and 532.10 eV.[43] The percentage of oxygen vacancies was found to be 22.41% and 31.22% for $Zn_{0.91}Eu_{0.09}MoO_4$ and $Zn_{0.88}Eu_{0.09}Li_{0.03}MoO_4$, respectively. This shows that there is an increase in the amount of oxygen vacancies upon co-doping with Li ions. These oxygen vacancies act as sensitizers, facilitating highly efficient radiative energy transfer to $Eu^{3+}$ ions by strong mixing of the charge transfer band (CTB), leading to enhanced luminescence.[44]

### 3.3. Solid state $^7$Li NMR

Fig. 3(a) presents the $^7$Li MAS-NMR spectra of $Zn_{(0.91-y)}Eu_{0.09}Li_yMoO_4$ ($y$ = 0.01, 0.03, and 0.05) phosphors confirming the incorporation of Li ions in the $ZnMoO_4$ lattice. Fig. 3(b) presents a zoomed-in view of the isotropic peak. All the samples exhibit two prominent peaks: one at approximately 3.6 ppm, which corresponds to diamagnetic Li sites in the sample, and another around −15.2 ppm, attributed to paramagnetic Li sites resulting from the presence of paramagnetic $Eu^{3+}$ sites. However, as the lithium concentration increases beyond 3 mol%, the $^7$Li NMR spectrum shows a higher intensity of the diamagnetic peak, as further discussed in Section 3.7.

### 3.4. FESEM analysis

Fig. 4 shows the detailed analysis of the $Zn_{0.88}Eu_{0.09}Li_{0.03}MoO_4$ phosphor to identify the morphology and homogeneity of the dopants. As revealed in Fig. 4(a), the morphology of the obtained sample was microparticles with irregular shapes and varying sizes. Fig. 4(b)–(e) illustrate the elemental mapping of Zn, Mo, O, and Eu, respectively. These images confirm the homogeneous distribution of all the elements across the agglomerated particles, indicating successful and even incorporation of $Eu^{3+}$ ions within the $ZnMoO_4$ matrix. Fig. 4(f) shows the EDS image, which highlights specific areas of the sample where the EDS spectrum was obtained. Fig. 4(g) shows the EDS

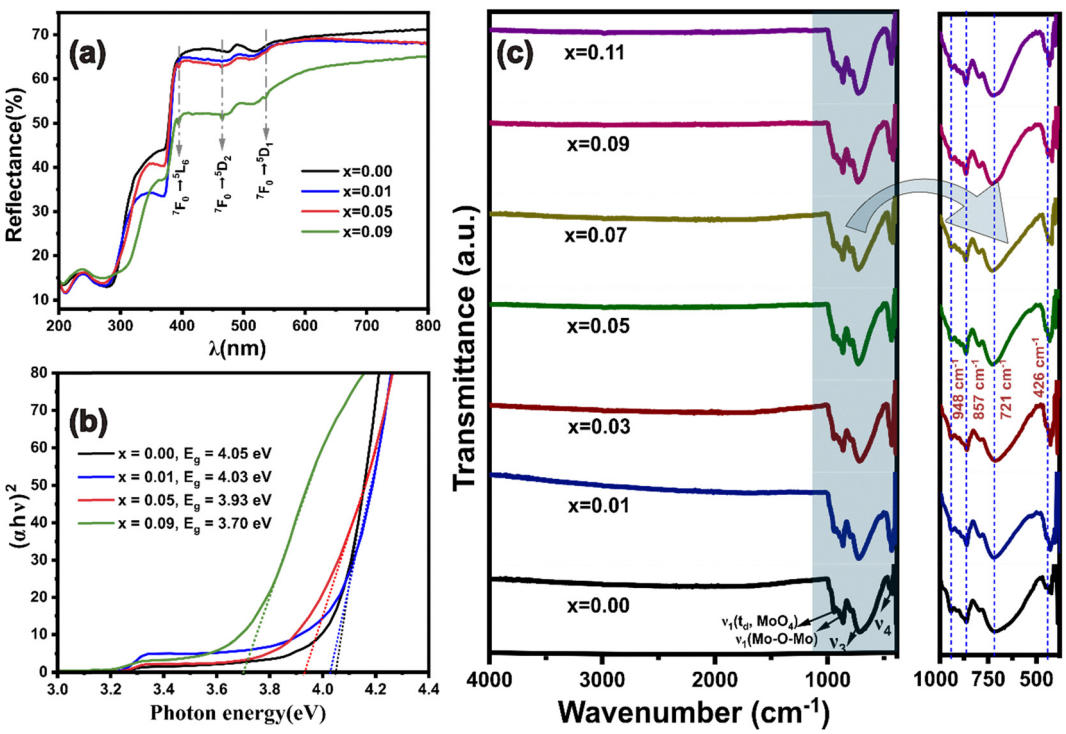


Fig. 5 (a) and (b) DRS spectra and Kubelka–Munk plot of $Zn_{(1-x)}Eu_xMoO_4$ ($x$ = 0.00, 0.01, 0.05, and 0.09) phosphors. (c) FTIR spectra of $Zn_{(1-x)}Eu_xMoO_4$ ($0.01 \leq x \leq 0.11$) phosphors.

spectrum, which reveals characteristic peaks corresponding to these elements, with no significant impurities detected. The Al, C, and Au peaks in the EDS spectrum likely result from the aluminium stub, carbon tape, and gold sputter coating used for conductivity during SEM analysis.[45]

### 3.5. UV DRS and FTIR

The diffuse reflectance spectroscopy (DRS) spectra of the $Zn_{(1-x)}Eu_xMoO_4$ phosphors were recorded in the 200–800 nm range, as shown in Fig. 5(a). According to Zhai *et al.*,[46] $ZnMoO_4$ exhibits two distinct absorption bands: one in the 250–310 nm range, corresponding to the transition of electrons from the valence band to the conduction band of $ZnMoO_4$, and another in the 310–390 nm range, which is associated with defects present in the $ZnMoO_4$ lattice. Fig. 5(a) clearly shows that doping with Eu ions increases the population density of defects, as indicated by the enhanced absorption in the 310–390 nm region. The sharp bands at 394 nm, 464 nm, and 536 nm are attributed to the $^7F_0 \rightarrow {}^5L_6$, $^7F_0 \rightarrow {}^5D_2$, and $^7F_0 \rightarrow {}^5D_1$ transitions of the $Eu^{3+}$ ion, respectively.[47] This confirms the successful incorporation of $Eu^{3+}$ ions into the $ZnMoO_4$ lattice.

The Kubelka–Munk theory[48] was employed to calculate the band gap of phosphor samples using the reflectance data.

$$\text{Kubelka} - \text{Munk function, } F(R_\infty) = \frac{k}{S} = \frac{(1-R_\infty)^2}{2R_\infty} \quad (2)$$

where $k$ and $S$ are absorption and scattering factors, respectively. While $R_\infty = \frac{R_{\text{sample}}}{R_{\text{reference}}}$ is the diffuse reflectance of the sample.

The bandgap energy of the samples can be calculated using the Tauc relation[49]

$$(\alpha h\nu)^{1/n} = B(h\nu - E_g) \quad (3)$$

where $\alpha$ is the energy-dependent absorption coefficient, $h\nu$ is the energy of the incident photon, $E_g$ is the band gap energy, and $B$ is a constant. Substituting $F(R_\infty)$ in place of $\alpha$ in eqn (2) yields eqn (3)

$$(F(R_\infty)\cdot h\nu)^{1/n} = B(h\nu - E_g) \quad (4)$$

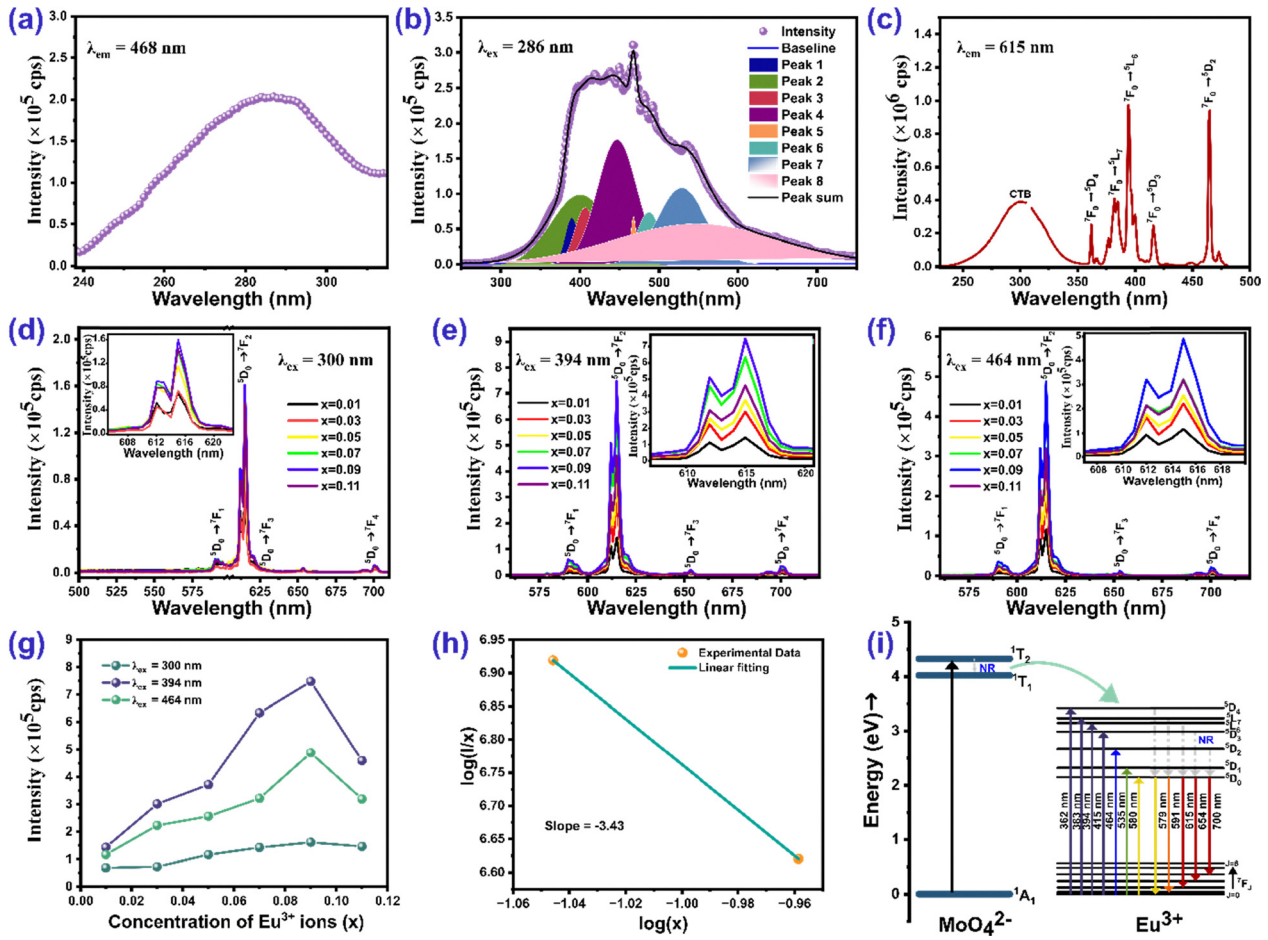


Fig. 6 (a) PL excitation and (b) PL emission spectra of the $ZnMoO_4$ host. (c) PLE spectrum of the $Zn_{0.91}Eu_{0.09}MoO_4$ phosphor ($\lambda_{em}$ = 615 nm). (d)–(f) PL emission spectra of $Zn_{(1-x)}Eu_xMoO_4$ ($0.01 \leq x \leq 0.11$) phosphors at an excitation wavelength of 300 nm, 394 nm, and 464 nm, respectively (the inset displays a magnified view of the $^5D_0 \rightarrow {}^7F_2$ emission peak). (g) PL emission intensity ($^5D_0 \rightarrow {}^7F_2$ emission peak at 615 nm) as a function of concentration of $Eu^{3+}$ ions at 300 nm, 394 nm, and 464 nm. (h) Plot of log(*x*) *vs.* log(*I*/*x*). (i) Schematic diagram depicting energy transfer from the host $ZnMoO_4$ to $Eu^{3+}$ ions.

Factor $n$ depends on the nature of electronic transitions and is equal to 0.5, 1.5, 2, or 3 for direct allowed, direct forbidden, indirect allowed, and indirect forbidden transitions, respectively.[50] $ZnMoO_4$ has been reported to have direct allowed electronic transition;[50] hence, $n$ equals 0.5 is used in the present study. Fig. 5(b) shows the graph of $(\alpha h\nu)^2$ *versus* $h\nu$, and extrapolating the straight line to $(\alpha h\nu)^2 = 0$ gives the value of band gap energy. The $E_g$ values estimated for the phosphors are between 4.05 eV and 3.70 eV and are in good agreement with the previously reported values.[50,51] The reduction in band gap with increasing dopant concentration is attributed to the formation of intermediate defect energy levels from $Eu^{3+}$ ions, facilitating electron transfer from $O^{2-}$ ions to these intermediate $Eu^{3+}$ orbitals.[52]

The infrared vibrational modes of the bonds in the $Zn_{(1-x)}Eu_xMoO_4$ ($0 \le x \le 0.11$) phosphors were analyzed using FTIR spectroscopy. The FTIR spectra, recorded in transmittance mode within the wavenumber range of 385 to 4000 $cm^{-1}$, are shown in Fig. 5(c). The phosphor samples showed prominent and identical IR absorption peaks at 948, 857, 727, and 426 $cm^{-1}$. These peaks correspond to the $\nu_1$ stretching of Mo–O in bridging Mo–O–Mo linkages, the $\nu_1$ stretching of $(MoO_4)^{2-}$ tetrahedra, the $\nu_3$ stretching of Mo–O, and the $\nu_4$ bending mode of Mo–O, respectively. The absence of any additional vibrational bands confirms the monophasic nature of the phosphors.

### 3.6. Photoluminescence properties

The PL excitation spectrum of the host $ZnMoO_4$ acquired at 468 nm emission wavelength is shown in Fig. 6(a). The excitation spectrum shows a ligand to metal charge transfer (LMCT) broad band centered at 286 nm, which corresponds to $O^{2-}$ to $Mo^{6+}$ charge transfer in the $[MoO_4]^{2-}$ groups of $ZnMoO_4$.[53] Fig. 6(b) exhibits the emission spectrum of $ZnMoO_4$ acquired at emission wavelength 286 nm. The emission peak is deconvoluted into several Gaussian peaks in the range of 300 to 750 nm. The peak in the UV emission range at around 389 nm corresponds to the recombination of free excitons *via* donor–acceptor pair transitions from the conduction band (CB) to the valence band (VB). The peak at 407 nm is ascribed to electron transitions from the lower edge of the conduction band to the zinc vacancy ($V_{Zn}$) level.[54] The blue emission at 447 nm arises from electron transitions from the donor level of zinc interstitials to the valence band.[55] The emission band at 487 nm can be associated with various types of distorted regular $MoO_4$ complexes.[56] The green luminescence bands observed between 520 and 550 nm can be attributed to electron transitions from deep oxygen vacancy levels to the top of the valence band.[54]

Fig. 6(c) shows the excitation spectra of the $Zn_{0.91}Eu_{0.09}MoO_4$ phosphor at 615 nm emission wavelength. The broad band in the range of 240–350 nm arises because of the contribution from different electronic transitions, which are (i) charge transfer from $O^{2-}$ to $Mo^{6+}$, (ii) charge transfer from the 2p orbital of $O^{2-}$ to the 4f orbital of $Eu^{3+}$, and (iii) inter valence charge transfer from $Eu^{3+}$ to $Mo^{6+}$.[57] The spectra contain other excitation peaks in the range of 350–500 nm arising due to the 4f–4f transition of the $Eu^{3+}$ ion. Among these transitions, the most intense ones are located at 394 nm ($^7F_0 \rightarrow {}^5L_6$) and 464 nm ($^7F_0 \rightarrow {}^5D_2$), and the less intense ones are located at 362 nm ($^7F_0 \rightarrow {}^5D_4$), 382 nm ($^7F_0 \rightarrow {}^5G_2$), and 416 nm ($^7F_0 \rightarrow {}^5D_3$).[37] Fig. 6(d)–(f) show the emission spectrum of the $Zn_{(1-x)}Eu_xMoO_4$ ($0 \le x \le 0.11$) phosphor at excitation wavelengths 300 nm, 394 nm, and 464 nm, respectively. The peak position remains the same, whereas there is variation in the emission intensities for both the excitation wavelengths. The most intense emission peak occurs at 615 nm, corresponding to the $^5D_0 \rightarrow {}^7F_2$ transition, and the other less intense peaks are at 590 nm ($^5D_0 \rightarrow {}^7F_1$), 653 nm ($^5D_0 \rightarrow {}^7F_3$) and 700 nm ($^5D_0 \rightarrow {}^7F_4$). The $^5D_0 \rightarrow {}^7F_1$ emission at 590 nm is a magnetic dipole transition (MDT) and is generally unaffected by changes in the local environment surrounding the $Eu^{3+}$ ion. In contrast, the $^5D_0 \rightarrow {}^7F_1$ emission at 615 nm is an electric dipole transition (EDT) and is highly sensitive to the local environment, including factors like symmetry and the local field around the $Eu^{3+}$ ion.[37,57] The significantly greater intensity of the $^5D_0 \rightarrow {}^7F_2$ transition at 615 nm (EDT) compared to the $^5D_0 \rightarrow {}^7F_1$ transition at 590 nm (MDT) in $ZnMoO_4$ suggests that $Eu^{3+}$ ions at the Zn site lack inversion symmetry, indicating a low local symmetry around the europium ion in $ZnMoO_4$. Fig. 6(g) shows that the emission intensity at 615 nm for all excitation wavelengths increases as the Eu ion concentration increases, reaching a peak at 9 mol% and then decreasing afterward.

To gain more insight into the concentration quenching of the $Zn_{(1-x)}Eu_xMoO_4$ ($0 \le x \le 0.11$) phosphors, the distance between $Eu^{3+}$ ions, was calculated using the following equation.[58]

$$R_C = \left(\frac{M}{\rho x_C N_A}\right)^{1/3} \quad (5)$$

where $R_C$ is the critical distance, $M$ and $\rho$ are the molecular weight and density of $ZnMoO_4$, $x_C$ is the critical concentration of the dopant ion, and $N_A$ is the Avogadro constant. Energy transfer *via* multipole–multipole interactions becomes significant when the critical distance between rare earth ions is greater than 0.5 nm, while exchange interactions dominate when this distance is below 0.5 nm.[58] In this case the critical distance was calculated to be 0.99 nm, indicating that concentration quenching occurs through multipolar interactions in this study. The electric multipolar interaction is of several types: dipole–dipole, dipole–quadrupole, and quadrupole–quadrupole interactions. To determine the dominant interaction type, the correlation between emission intensity and activator concentration is examined, as described by Van Uitert's equation below.[59]

$$I = \frac{x}{K\left[1 + \beta(x)^{\frac{\theta}{3}}\right]} \quad (6)$$

where $I$ is the emission intensity, $x$ is the concentration of $Eu^{3+}$ ions, and $K$ and $\beta$ are constants specific to a given host under identical excitation conditions. $\theta = 3$ represents exchange interaction, $\theta = 6$, 8, and 10 correspond to dipole–dipole, dipole–quadrupole, and quadrupole–quadrupole interactions, respectively.[60] Eqn (5) can be transformed into the equation

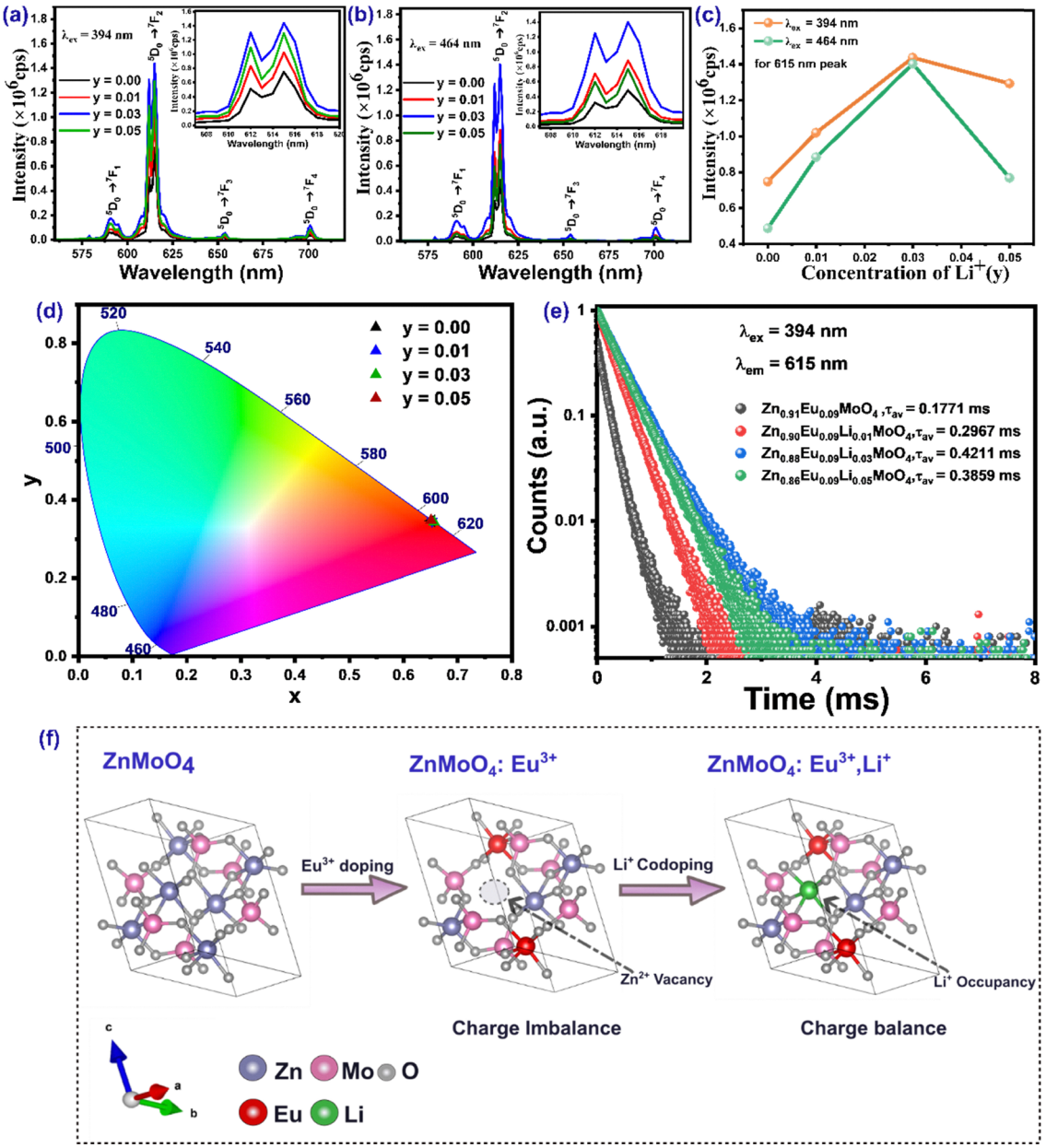


Fig. 7 PL emission spectra of the $Zn_{(0.91-y)}Eu_{0.09}Li_yMoO_4$ ($0 \le y \le 0.05$) phosphors at (a) 394 nm and (b) 464 nm excitation wavelengths. (c) PL emission intensity ($^5D_0 \rightarrow {}^7F_2$ emission peak at 615 nm) as a function of concentration of $Eu^{3+}$ ions at 394 nm and 464 nm. (d) CIE 1931 chromaticity diagram (at 394 nm) and (e) PL decay curve for the $Zn_{(0.91-y)}Eu_{0.09}Li_yMoO_4$ ($0 \le y \le 0.05$) phosphors. (f) Schematic representation for charge compensation by introduction of $Li^+$ in $ZnMoO_4$:$Eu^{3+}$ phosphors.

shown below:

$$\log\left(\frac{I}{x}\right) = K' - \frac{\theta}{3}\log(x) \quad (7)$$

Fig. 6(h) represents the plot between $\log\left(\frac{I}{x}\right)$ *vs.* $\log(x)$. The critical concentration of $Eu^{3+}$ was determined to be 9 mol%. The dependence of the emission intensity of the $ZnMoO_4$:$xEu^{3+}$ phosphor excited at 394 nm as a function of the corresponding concentration of $Eu^{3+}$ for concentration greater than the critical concentration ($x \ge 0.09$) was evaluated. The value of $\theta$ can be determined from the slope ($-\theta/3$) of the plot, which was found to be 10.3, close to 10. This suggests that the energy migration between $Eu^{3+}$ ions is primarily due to quadrupole–quadrupole interactions.

The energy transfer mechanism from the host $ZnMoO_4$ to $Eu^{3+}$ ions is depicted in the schematic diagram in Fig. 6(i). Upon excitation at 286 nm, an electron in the oxygen 2p state ($^1A_1$) is excited to the $^1T_2$ level of the molybdenum 4d state in $MoO_4^{2-}$, after which it relaxes to the $^1T_1$ excited state. The energy gained by $MoO_4^{2-}$ is then transferred to the $^5D_4$ or higher energy levels of the $Eu^{3+}$ ions within the host lattice *via* a

resonance process.[61] Upon excitation at 300 nm (charge transfer band), the emission spectra shown in Fig. 6(d) exclusively contain very sharp peaks corresponding to $Eu^{3+}$. Compared with the emission peaks of $Eu^{3+}$, the intrinsic blue-green emission from $MoO_4^{2-}$ groups is very weak, suggesting the existence of efficient energy transfer from the $MoO_4^{2-}$ cluster to the doped $Eu^{3+}$ ion in $ZnMoO_4$:Eu.

### 3.7. Photoluminescence properties of $Li^+$ codoped $Eu^{3+}$ $ZnMoO_4$

To further investigate the effect of alkali ion co-doping on the Eu-doped phosphor materials, $Zn_{0.91}Eu_{0.09}MoO_4$ was co-doped with $Li^+$ at concentrations of 1 mol%, 3 mol%, and 5 mol%. The PL emission spectra of the $Zn_{(0.91-y)}Eu_{0.09}Li_yMoO_4$ ($0 \leq y \leq 0.05$) phosphors at 394 nm and 464 nm excitation wavelengths are shown in Fig. 7(a) and (b), respectively. It can be clearly seen that the spectral features (such as shape and position) remain unchanged even after $Li^+$ co-doping. However, as shown in Fig. 7(c), the emission intensity at both excitation wavelengths increased with $Li^+$ co-doping up to 3 mol%, after which a decline was observed at 5 mol% $Li^+$ co-doping. A nearly twofold increase in PL intensity is observed for the $Zn_{0.88}Eu_{0.09}Li_{0.03}MoO_4$ phosphor, along with a rise in quantum yield from 14.5% to 27.2%. This enhancement at lower $Li^+$ concentrations is likely due to the charge compensation effect.[62] When $Eu^{3+}$ is introduced into the $ZnMoO_4$ matrix, it replaces $Zn^{2+}$ ions, creating an additional positive charge with each substitution. These extra positive charges repel one another, which limits the further incorporation of $Eu^{3+}$ ions into the host lattice. Excess $Eu^{3+}$ ions located outside the lattice positions can also serve as luminescence quenching sites. As shown by the schematic representation in Fig. 7(f), to maintain overall charge neutrality, two $Eu^{3+}$ ions substitute for three $Zn^{2+}$ ions within the $ZnMoO_4$ matrix, resulting in the formation of a $Zn^{2+}$ vacancy $\left(V''_{Zn}\right)$, $3Zn^{\times}_{Zn} \rightarrow 2Eu^{\bullet}_{Zn} + V''_{Zn}$. These $Zn^{2+}$ vacancies act as defect sites, leading to reduced overall luminescence intensity due to increased energy transfer from luminescent centers to vacancy defects. With the incorporation of $Li^+$ ions, charge balance is achieved *via* the reaction, $2Zn^{\times}_{Zn} + Eu^{3+} + Li^+ \rightarrow Eu^{\bullet}_{Zn} + Li'_{Zn}$. Thus, the addition of $Li^+$ lowers the probability of non-radiative transitions and significantly improves radiative transfer efficiency. However, because the ionic radii of the host metal and the alkali metal ion are different, even though the charge imbalance is addressed, alkali metal ions cannot fully resolve the volume imbalance issue. The problem of volume imbalance can be neglected only within a specific range of alkali metal ion concentration. As a result, when the $Li^+$ doping concentration exceeds 3 mol%, it causes distortion of the crystal lattice, which subsequently reduces the phosphor's crystallinity and leads to a decrease in luminescence intensity.

The formation of oxygen vacancies, which occurs when $Zn^{2+}$ is replaced by $Li^+$, is another crucial factor influencing the PL intensity of the $ZnMoO_4$:$Eu^{3+}$,$Li^+$ phosphors. These oxygen vacancies are generated on the surface of the phosphor and function as sensitizers. Fig. 2(f) represents a notable increase in the number of oxygen vacancies in the case of co-doping with 3 mol% Li ions. The transfer of energy from the host to the $Eu^{3+}$ ions through these sensitizers results in a substantial overlap of the charge transfer states. This significant overlap enhances the oscillator strength of the optical transition, thereby increasing the PL intensity.[63] Lattice modification occurs through the formation of Eu···O···Li clusters, where the local field around the europium ion is altered due to a redistribution of electron density around the oxygen ion. This redistribution causes an increased pull of electrons toward the $Eu^{3+}$ ion.[64] The paramagnetic shift in the Li spectrum shown in Fig. 3 can be attributed to the formation of these clusters. The increase in the diamagnetic peak with increasing Li concentration could be indicative of a saturation point where excessive lithium ions start occupying sites away from $Eu^{3+}$ ions.

The CIE chromaticity diagram is a valuable tool for assessing phosphor color emissions, where each emission is plotted based on its $x$ and $y$ chromaticity coordinates. In this study, the host $ZnMoO_4$ phosphor exhibits emission in the blue region of the CIE diagram as shown in Fig. S2 (ESI†), indicative of its characteristic blue luminescence. As shown in Fig. 7(d), on doping with $Eu^{3+}$, the emission shifts to the red region, reflecting the influence of $Eu^{3+}$ ions in altering the color output. Interestingly, further co-doping with $Li^+$ ions in the $ZnMoO_4$:9%$Eu^{3+}$ phosphor influences the chromaticity coordinates, leading to an increase in the $x$-coordinate and a decrease in the $y$-coordinate. This shift suggests an enhancement in color purity for the $Li^+$ co-doped nanophosphor, as the changes in the coordinates correspond to a more refined emission color within the red spectrum. This chromatic adjustment highlights the role of $Li^+$ co-doping in improving the visual quality of red-emitting phosphors by fine-tuning their chromatic properties. The color purity of the synthesized phosphors was calculated using the following equation.[65]

$$\text{Color purity} = \frac{\sqrt{(x_s - x_i)^2) + (y_s - y_i)^2}}{\sqrt{(x_d - x_i)^2) + (y_d - y_i)^2}} \quad (8)$$

Here, ($x_s$, $y_s$) represent the sample point coordinates, ($x_d$, $y_d$) denote the coordinates of the dominant wavelength, and ($x_i$, $y_i$) correspond to the illuminant point coordinates. In this study, with ($x_d$, $y_d$) set to (0.68, 0.32) for the dominant wavelength (615 nm) and ($x_i$, $y_i$) set to (0.315, 0.329) for the illuminant point, the color purities for the 9%$Eu^{3+}$ and 9%$Eu^{3+}$, 3%$Li^+$ co-doped $ZnMoO_4$ phosphors are calculated as 92.42% and 93.60%, respectively. McCamy's approximation was utilized to calculate the CCT values of the phosphors.[65]

$$\text{CCT} = -449n^3 + 3525n^2 - 6823n + 5520.33 \quad (9)$$

In this context, $n$ is calculated as $n = \frac{(x - x_e)}{(y - y_e)}$, with the chromaticity epicenter defined at $x_e = 0.3320$ and $y_e = 0.1858$ for the 615 nm emission. Table S2 (ESI†) presents the color coordinates, CCT values and color purity for all $ZnMoO_4$ phosphors doped with $Eu^{3+}$ and co-doped with $Eu^{3+}$ and $Li^+$. The measured chromaticity coordinates of our phosphor closely approach the

ideal red point (0.670, 0.330) and outperform those of the commercial $Y_2O_2S:Eu^{3+}$ phosphor, which are (0.622, 0.351).[66]

The decay profiles of $Zn_{(0.91-y)}Eu_{0.09}Li_yMoO_4$ ($0 \le y \le 0.05$) phosphors are presented in Fig. 7(e) with an excitation wavelength of 394 nm and emission wavelength of 615 nm. For the $^5D_0 \rightarrow {}^7F_2$ transition, the decay curves of the phosphors are modeled using a bi-exponential function expressed as[67]

$$I(t) = A_1 e^{(-t/\tau_1)} + A_2 e^{(-t/\tau_2)} \quad (10)$$

Here, $I(t)$ denotes the luminescence intensity at a given time $t$, with $\tau_1$ and $\tau_2$ as the decay time components, and $A_1$ and $A_2$ as the respective contributions to each decay component. For bi-exponential decay, the average lifetime is expressed as follows:[68]

$$\tau_{av} = \frac{A_1\tau_1^2 + A_2\tau_2^2}{A_1\tau_2 + A_2\tau_2} \quad (11)$$

The average lifetimes of the phosphors vary with the concentration of co-doped $Li^+$ ions. As the $Li^+$ concentration increases up to $y$ = 3 mol%, the average lifetime reaches a peak value of 0.42 ms, after which it slightly decreases with further increases in $Li^+$ concentration. The increase in lifetime due to $Li^+$ co-doping suggests a reduction in surface defects and nonradiative transitions within the co-doped phosphor. The millisecond-scale lifetime of the phosphors demonstrates their potential for practical lighting applications.

### 3.8. Judd–Ofelt analysis

Judd–Ofelt (JO) analysis is a crucial method to evaluate the luminescence properties and quantify the electronic transitions in the phosphors. The JO parameters ($\Omega_2$, $\Omega_4$) were extracted from the photoluminescence emission spectra, providing a detailed understanding of the local environment and asymmetry around the $Eu^{3+}$ ions in the $ZnMoO_4$ phosphor. The parameter $\Omega_2$ reflects the extent of asymmetry and covalency in the ligand field, while $\Omega_4$ correlates with the rigidity of the host lattice. The parameter $\Omega_6$ could not be obtained due to the absence of the $^5D_0 \rightarrow {}^7F_6$ transition. The radiative emission rate ($A_{0\text{–}J}$) for $^5D_0 \rightarrow {}^7F_J$ ($J$ = 1, 2, 4) transitions is determined by the integrated emission intensity ($I_{0\text{–}J}$) and corresponding transition energy ($h\nu_{0\text{–}J}$), correlating emission characteristics to radiative properties using the following equation:[37]

$$A_{0-J} = \frac{I_{0-J}}{I_{0-1}}\frac{h\nu_{0-1}}{h\nu_{0-J}}A_{0-1} \quad (12)$$

The magnetic dipole radiative emission rate ($A_{0\text{–}1}$) is considered constant, as it is unaffected by the crystal field, with a typical value of 50 $s^{-1}$. The radiative emission rates $A_{0\text{–}J}$ are related to the Judd–Ofelt (J–O) intensity parameters as follows:[69]

$$A_{0-J} = 64\frac{\pi^4 e^2}{3h\lambda^3}\frac{1}{4\pi\epsilon_0}\chi\sum_{J=2,4}\Omega_J\left\langle {}^5D_0\middle|U^{(J)}\middle|{}^7F_2\right\rangle^2 \quad (13)$$

In this context, $\chi$ is the Lorentz correction factor, which depends on the refractive index of the host matrix. The squared reduced matrix elements, $\langle {}^5D_0|U^{(J)}|{}^7F_{2,4}\rangle^2$, are intrinsic properties of $Eu^{3+}$ ions and remain unaffected by the local chemical environment. For the current study, these values are $\langle {}^5D_0|U^{(2)}|{}^7F_2\rangle^2$ = 0.0032 and $\langle {}^5D_0|U^{(4)}|{}^7F_4\rangle^2$ = 0.0023, corresponding to the $^5D_0$–$^7F_2$ and $^5D_0$–$^7F_4$ transitions, respectively.[70] The total radiative transition probability ($A_T$), radiative lifetime ($\tau_{rad}(\psi_J)$), and branching ratio ($\beta(\psi_J)$) for emissions from an excited state to lower energy levels can be calculated using the following equations:[71]

$$A_{rad}(\psi_J) = \sum_{J=2,4} A_{0-J} \quad (14)$$

$$\tau_{rad}(\psi_J) = \frac{1}{A_{rad}} \quad (15)$$

$$\beta(\psi_J) = \frac{A_{0-J}}{A_{rad}(\psi_J)} \quad (16)$$

The asymmetric ratio ($R$) is calculated using the ratio of electric dipole to magnetic dipole transition integrated emission intensities as follows:[37]

$$R = \frac{\int I_{ED}\cdot d\lambda}{\int I_{MD}\cdot d\lambda} \quad (17)$$

From Table S3 (ESI†), it is evident that $\Omega_2$ is greater than $\Omega_4$ across all doping and co-doping concentrations, suggesting a covalent bonding nature between $Eu^{3+}$ and $O^{2-}$ ligands, as well as asymmetry in the local environment surrounding the $Eu^{3+}$ ions in the $ZnMoO_4$ matrix. The dominance of the $^5D_0 \rightarrow {}^7F_2$ transition (615 nm) in the PL spectra is attributed to the higher $\Omega_2$ value, highlighting the covalent nature of the Eu–O bond and the asymmetry around the $Eu^{3+}$ ions. The asymmetric ratio, greater than 1, further confirms the existence of asymmetric sites for $Eu^{3+}$, leading to strong covalent interactions with the surrounding ligands. This finding suggests that the $^5D_0 \rightarrow {}^7F_2$ transition is primarily responsible for the $Eu^{3+}$ emission, as supported by its higher branching ratio compared to other transitions.[72] Table S3 (ESI†) presents the comprehensive analysis of the Judd–Ofelt parameters. Table 1 summarizes the Judd–Ofelt intensity parameters for $Eu^{3+}$ across different host matrices. A comparative evaluation of the Judd–Ofelt intensity parameters ($\Omega_2$, $\Omega_4$) reveals that the values obtained in the present study are significantly higher than those reported for many conventional $Eu^{3+}$-doped hosts. The elevated $\Omega_2$ values in our phosphors indicate a highly asymmetric and covalent local environment around $Eu^{3+}$ ions. These findings suggest that $ZnMoO_4$ is a promising host for enhancing electric dipole transitions, thus improving radiative efficiency.

Table 1 Judd–Ofelt intensity parameters ($\Omega_2$ and $\Omega_4$) for $Eu^{3+}$ across various host matrices

| Phosphor | J–O intensity parameters ($\times 10^{-20}$ $cm^2$) $\Omega_2$ | $\Omega_4$ | Ref. |
|---|---|---|---|
| $Na_2ZnP_2O_7:0.01Eu^3$ | 3.37 | 1.22 | Fhoula *et al.*[74] |
| $KBaScSi_3O_9:Eu^{3+}$ | 1.05 | 0.30 | Nagaraj *et al.*[75] |
| $Y_2O_3:Eu^{3+}$ | 6.06 | 0.08 | Patwardhan *et al.*[76] |
| $NiNb_2O_6:Eu^{3+}$ | 10.02 | 2.73 | İlhan *et al.*[77] |
| $NaMgF_3:Eu^{3+}$ | 34.9 | 6.03 | Nalumaga *et al.*[78] |
| $ZnMoO_4:0.09Eu^{3+}$ | 38.79 | 7.43 | Present work |
| $ZnMoO_4:0.09Eu^{3+},0.03Li^+$ | 31.12 | 7.04 | Present work |

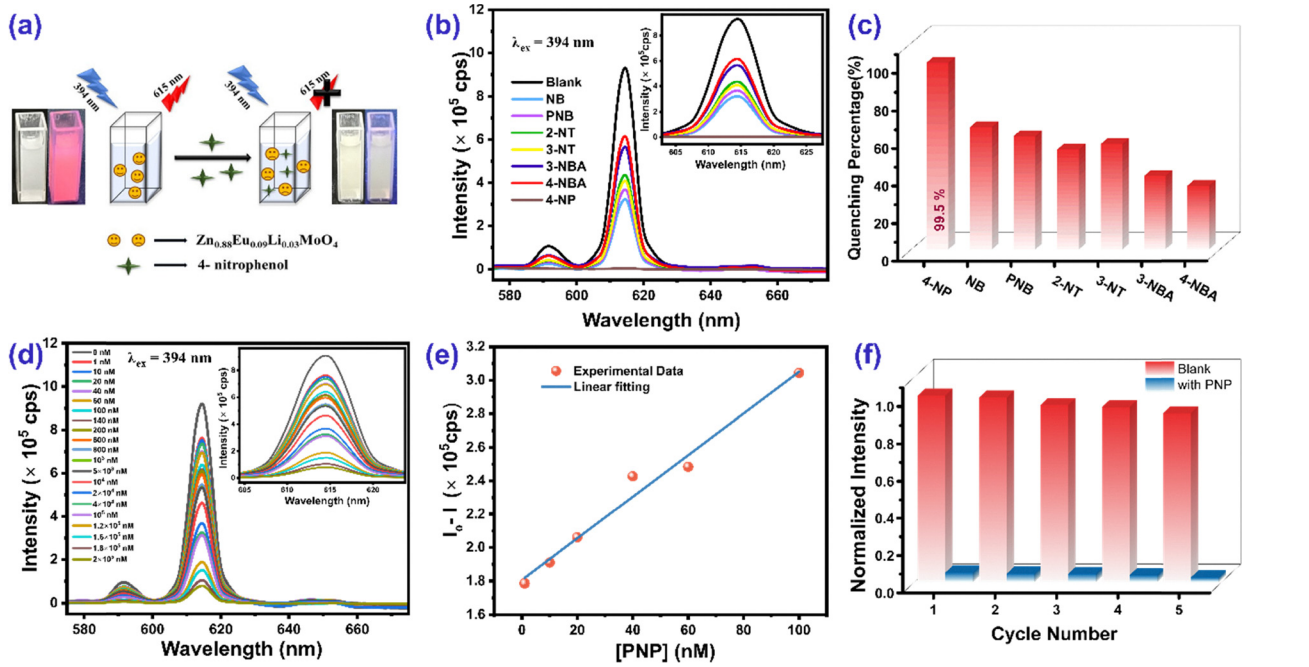


Fig. 8 (a) Schematic illustration for 4-nitrophenol sensing using the $Zn_{0.88}Eu_{0.09}Li_{0.03}MoO_4$ (ZELMO) phosphor. (b) The luminescence intensity of ZELMO dispersed in aqueous solutions of different nitroaromatic compounds excited with 394 nm. (c) Bar diagram to show the nitro aromatic compound selectivity of ZELMO in deionized water. (d) The luminescence response of ZELMO to different concentrations of 4-NP (0–200 μM) in deionized water. (e) Plot of $I_0 - I$ *versus* increasing concentrations of 4-NP to calculate the limit of detection. (f) Original (red) and quenched (blue) luminescence intensity of ZELMO at 615 nm recycled after sensing experiments for 4-NP.

The stimulated emission cross-section ($\sigma_e$) is a critical parameter that characterizes the efficiency of energy extraction from a lasing medium. It is determined using the following formula:[73]

$$\sigma_e(\lambda_p) = \frac{\lambda_p^4}{8\pi c n^2 \Delta\lambda_{eff}} A_{rad}(\psi_J) \quad (18)$$

Here, $\lambda_p$ represents the emission peak wavelength, $c$ denotes the speed of light, and $\Delta\lambda_{eff}$ refers to the effective emission bandwidth of the transition. For $Eu^{3+}$-activated $ZnMoO_4$ phosphors, the $\sigma_e$ values follow the trend $^5D_0 \rightarrow {}^7F_2 > {}^7F_4 > {}^7F_1$ as presented in Table S4 (ESI†). The highest $\sigma_e$ value, measured at 88.85 × $10^{-22}$ $cm^2$ for the $^5D_0 \rightarrow {}^7F_2$ transition in $Zn_{0.97}Eu_{0.03}MoO_4$, highlights the exceptional capability of the material for energy extraction. Table S5 (ESI†) presents a comparative analysis of the stimulated emission cross-section ($\sigma_e$) values reported for $^5D_0 \rightarrow {}^7F_2$ transition for $Eu^{3+}$-doped phosphors in similar hosts $CaMoO_4$ and $BaWO_4$. This significant stimulated emission cross-section is a key indicator of enhanced lasing efficiency. Its high value supports the achievement of low-threshold and high-gain laser performance, emphasizing the phosphor's suitability for advanced laser applications and its potential for efficient and reliable laser operation.[69]

The product of the stimulated emission cross-section ($\sigma_e$) and effective bandwidth ($\Delta\lambda_{eff}$) is an important parameter for predicting the amplification bandwidth of optical systems. Higher product values lead to enhanced amplifier performance. For $ZnMoO_4$:$Eu^{3+}$ (3 mol%), the maximum gain bandwidth observed was 26.15 × $10^{-28}$ $cm^3$ for the $^5D_0 \rightarrow {}^7F_2$ transition. Additionally, the product of radiative lifetime ($\tau_{rad}$) and $\sigma_e$ highlights substantial optical gain, establishing the $^5D_0 \rightarrow {}^7F_2$ transition as a robust candidate for efficient laser applications and advanced display technologies.

### 3.9. Selective sensing of nitro aromatic compounds

In this study, selective sensing of nitroaromatic compounds was explored using phosphor emission quenching as a detection method. The $Zn_{0.88}Eu_{0.09}Li_{0.03}MoO_4$ (ZELMO) phosphor exhibited the highest emission intensity of all the synthesized samples. Consequently, this sample was selected for further sensing investigations.

Fig. 8(a) provides a schematic illustration of the quenching mechanism, where adding *para*-nitrophenol (PNP) to an aqueous phosphor solution causes a marked reduction in phosphor emission on excitation at 394 nm. Fig. 8(b) shows the emission spectra at 394 excitation wavelength for a blank aqueous phosphor solution and solutions containing various nitroaromatic compounds, specifically nitrobenzene (NB), *para*-nitrobenzaldehyde (PNB), 3-nitrotoluene (3-NT), 2-nitrotoluene (2-NT), 3-nitrobenzoic acid (3-NBA), 4-nitrobenzoic acid (4-NBA), and *para*-nitrophenol (4-NP). Each compound was tested at a concentration of 50 mM, and PNP demonstrated a stronger quenching effect than other nitro aromatics.

Fig. 8(c) illustrates this selectivity in a bar graph, highlighting PNP's pronounced quenching effect on phosphor emission intensity relative to other compounds. Fig. 8(d) presents the quenching response of the phosphor across a concentration

Table 2 Materials for detection of *para* nitrophenol

| Sensing probe | Detection method | Detection limit (nM) | Ref. |
|---|---|---|---|
| rGO–$MoS_2$/$Fe_3O_4$ | Electrochemical | 800 | Kalia *et al.*[79] |
| Si NPs | Fluorescence | 74 | Liu *et al.*[80] |
| rGO–HNT–AgNPs | Electrochemical | 48.6 | Hwa *et al.*[81] |
| $Cu_{0.5}$–$Fe_3O_4$@VXC-72/GCE | Electrochemical | 65 | Cao *et al.*[82] |
| $FeSe_2$ | Electrochemical | 30 | Chang *et al.*[83] |
| PVP@BP | Electrochemical | 28 | Shen *et al.*[84] |
| Si-CDs | Fluorescence | 23.45 | Zhu *et al.*[85] |
| $Zn_{0.88}Eu_{0.09}Li_{0.03}MoO_4$ phosphor | Fluorescence | 12 | Present work |

range of PNP from 1 nM to 200 μM, showing a decrease in emission intensity with increasing PNP concentration. To calculate the limit of detection (LOD) of PNP, the difference in fluorescence intensity ($I_0 - I$) was plotted against the PNP concentration, as shown in Fig. 8(e). Here, $I_0$ represents the fluorescence intensity of the blank (solvent without PNP), and $I$ is the intensity of the PNP solution at varying concentrations. The detection limit for *p*-NP was calculated as 12 nM using the $3\sigma$/slope method, where $\sigma$ represents the standard deviation of the blank measurements.[86] This detection limit is lower than the maximum allowable concentration of 0.43 μM in drinking water set by the US Environmental Protection Agency (EPA). Additionally, the performance of phosphors as a fluorescent sensor for *p*-NP was evaluated against other previously reported analytical methods, with comparative results summarized in Table 2. Finally, Fig. 8(f) examines the recyclability of the phosphor sensor over five sensing cycles with and without PNP, demonstrating minimal loss in emission intensity, indicating the phosphor's robustness and potential for repeated use in PNP detection.

### 3.10. Mechanism of sensing

The fluorescence quenching process can occur through several mechanisms, including dynamic quenching, static quenching, the inner filter effect (IFE), Förster resonance energy transfer (FRET), photo-induced electron transfer, aggregation-caused quenching (ACQ), collisional quenching, and ground-state complex formation, among others.[87] To identify the most likely quenching pathways in this study, we analyzed the absorption spectra of the nitroaromatic compounds (Fig. 9(a)) and the excitation and emission spectra of the phosphor.

The lack of overlap between the absorption spectrum of *para*-nitrophenol (PNP) and the emission spectrum of the phosphor, as shown in Fig. 9(b), indicates that Förster resonance energy transfer (FRET) is not involved in the quenching mechanism. In contrast, the emission spectrum of the phosphor shows substantial overlap with the absorption spectrum of PNP, pointing to the inner filter effect (IFE) as the primary mechanism for fluorescence quenching.

To further confirm the quenching pathway, time-resolved fluorescence decay experiments were performed. ZELMO exhibits a lifetime of 0.258 ms in the absence of PNP, which decreases only marginally to 0.246 ms upon addition of PNP (Fig. S3, ESI†). This minimal change in lifetime indicates that PNP does not participate in excited-state interactions with the phosphor, but instead reduces the detected fluorescence intensity through an inner filter effect.

The inner filter effect (IFE) occurs when the emission or excitation wavelengths of a fluorescent phosphor overlap with the absorption spectrum of a coexisting species (in this case, PNP). This overlap enables the absorber (PNP) to attenuate the fluorescence signal of the phosphor by absorbing emitted photons, effectively "filtering" the detected fluorescence without direct molecular interactions between the sensor and the analyte. IFE is particularly advantageous for sensing applications because it does not require physical binding or chemical modifications to

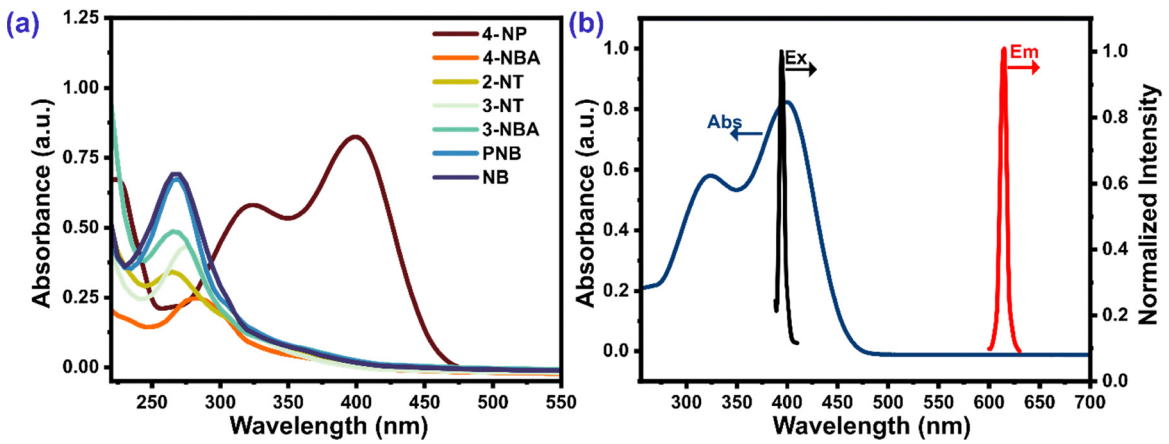


Fig. 9 (a) UV-vis absorption spectra of different nitroaromatic compounds. (b) UV-vis absorption spectra of 4-NP and excitation and emission spectra of the ZELMO phosphor dispersed in deionized water.

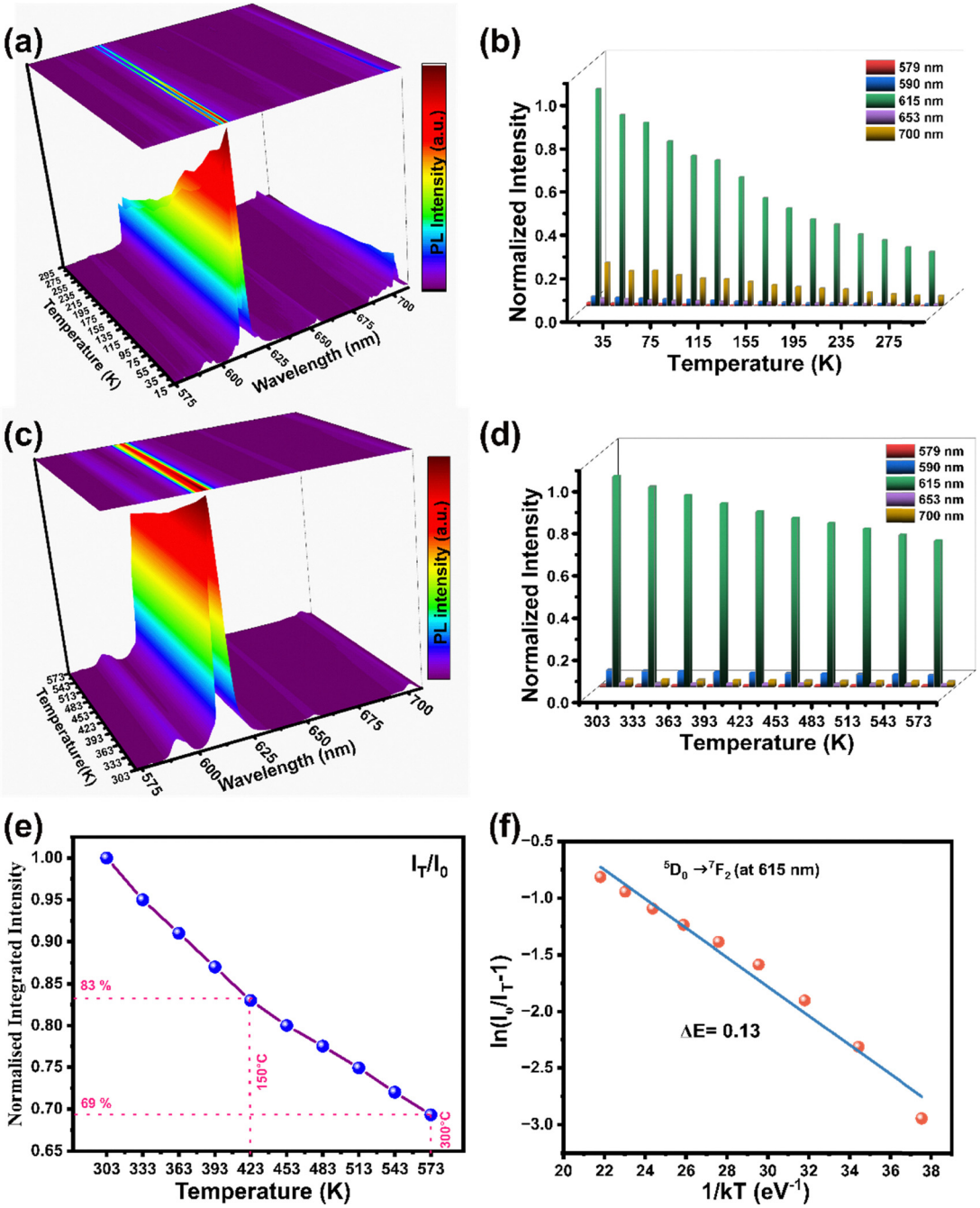


Fig. 10 3D color contour of ZELMO in the temperature range (a) 15 K to 295 K and (c) 303 K to 573 K. Bar diagram illustrating the intensity variation of four major peaks as a function of temperature in the temperature range (b) 15 K to 295 K and (d) 303 K to 573 K. (e) Variation of normalized integrated intensity with temperature (303 K to 573 K). (f) $\ln\left(\frac{I_0}{I_T}-1\right)$ *vs.* $1/kT$ plot for calculation of the activation energy.

the probe, unlike mechanisms such as static or dynamic quenching. As a result, IFE-based sensing is often simpler and more robust, avoiding structural or chemical perturbations of the probe, thus enhancing sensor stability and reusability.[88]

### 3.11. Thermal stability

The thermal stability of ZELMO was investigated by analyzing its emission behavior across a wide temperature range. The 3D color contour emission spectra at 394 nm excitation wavelength for the temperature range 15 K to 295 K (Fig. 10(a)) showed that the peak positions remained unchanged, indicating stable emission characteristics. However, a reduction in emission intensity was observed as the temperature increased. This observation was further confirmed by the normalized intensity bar graph (Fig. 10(b)), which demonstrated a steady decrease in emission intensities at 579 nm, 590 nm, 615 nm, 653 nm, and

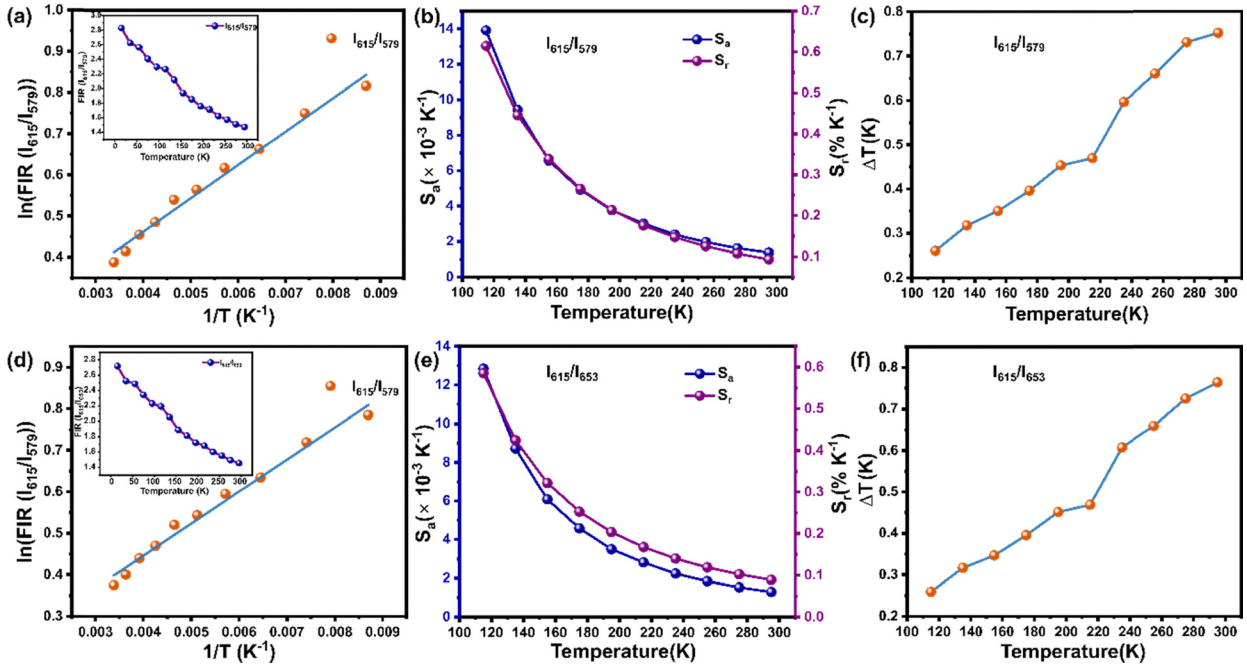


Fig. 11 ln(FIR) *vs.* 1/*T* plot for (a) $I_{615}/I_{579}$, and (d) $I_{615}/I_{653}$ (the inset shows the respective FIR *vs.* *T* plots). Temperature dependence of absolute sensitivity ($S_a$) and relative sensitivity ($S_r$) for (b) $I_{615}/I_{579}$, and (e) $I_{615}/I_{653}$. Variations in temperature uncertainty ($\Delta T$) with temperature for (c) $I_{615}/I_{579}$, and (f) $I_{615}/I_{653}$.

700 nm within the same temperature range. In the higher temperature range of 303 K to 573 K, both the 3D contour plot (Fig. 10(c)) and the associated bar graph (Fig. 10(d)) showed a persistent decrease in emission intensity, with no shift in peak positions. This behavior suggests that the phosphor exhibits resistance to thermal quenching. The normalized integrated intensity *versus* temperature graph (Fig. 10(e)) further reveals that the phosphor retains 83% of its luminescence at 423 K and 69% at 573 K, highlighting its remarkable thermal stability.

The activation energy ($\Delta E$) for the thermal deactivation process was calculated using the following equation:[89]

$$I_t = \frac{I_0}{1 + A e^{(-\Delta E/kT)}} \quad (19)$$

Here, $A$ is a constant, $k$ is Boltzmann's constant, with a value of $8.629 \times 10^{-5}$ eV $K^{-1}$, $I_0$ is the initial emission intensity at room temperature, $I_t$ is the emission intensity at varying temperatures, and $\Delta E$ denotes the activation energy associated with thermal quenching. The activation energy, $\Delta E$, can be determined by plotting the $\ln(I_0/I_t - 1)$ *versus* $1/kT$ curve as shown in Fig. 10(f). The slope of the fitted line corresponds to the activation energy, $\Delta E$, which was determined to be 0.13 eV.

### 3.12. Low-temperature optical thermometry

This study explores the potential of the ZELMO phosphor for non-contact optical thermometry in the temperature range of 15 K to 295 K. The temperature-dependent photoluminescent properties of this phosphor were analyzed using the fluorescence intensity ratio (FIR) method, focusing on its emission bands at 579 nm ($^5D_0 \rightarrow {}^7F_0$), 615 nm ($^5D_0 \rightarrow {}^7F_2$), and 653 nm ($^5D_0 \rightarrow {}^7F_3$). Two specific fluorescence intensity ratios, 615 nm/579 nm, and 615 nm/653 nm, were selected for the subsequent calculations. The relationship between the FIR and temperature was determined using the following expression:[90]

$$\mathrm{FIR} = \frac{I_1}{I_2} = B + C e^{(-\Delta E/kT)} \quad (20)$$

Here, $I_1$ represents the intensity of the 615 nm emission peak, while $I_2$ corresponds to the intensities of the 579 nm, and 653 nm emission peaks. $k$ is Boltzmann's constant, and $B$ and $C$ denote the proportionality constant and the offset parameter, respectively. Insets in Fig. 11(a) and (d) present the FIR variations with temperature, showing a predictable trend. A linear relationship was observed between ln(FIR) and $1/T$ (Fig. 11(a) and (d)), with the slopes corresponding to $\Delta E/k$. The calculated values of $\Delta E/k$ were 81.26, and 77.36 for the two ratios 615 nm/579 nm, and 615 nm/653 nm, respectively. $\Delta E$ for the ratio 615 nm/579 nm corresponds to the energy difference between the $^5D_0 \rightarrow {}^7F_2$ and $^5D_0 \rightarrow {}^7F_0$ transitions, while $\Delta E$ for the ratio 615 nm/653 nm corresponds to the energy difference between the $^5D_0 \rightarrow {}^7F_2$ and $^5D_0 \rightarrow {}^7F_3$ transitions.

These intensity ratios were selected to examine how the dominant electric dipole transition of $Eu^{3+}$ at 615 nm varies relative to other $Eu^{3+}$ transitions as a function of temperature. With increasing temperature, a gradual decrease in the FIR ratio is observed. This trend is attributed to thermal expansion of the lattice, which increases the $Eu^{3+} \rightarrow O^{2-}$ bond distance, thereby enhancing the covalency of the local environment.[91] The increased covalency alters the asymmetry around the $Eu^{3+}$ site, leading to a reduction in the relative intensity of the electric dipole transition and, consequently, a decrease in the FIR ratio. Moreover, this behavior supports the notion that

Table 3 Comparison of the calculated $S_r$, and $S_a$ thermometric parameters for $Eu^{3+}$ doped samples in different host materials

| Material | Temperature range (K) | $S_a$-max ($\times 10^{-3}$ $K^{-1}$) | $S_r$-max (% $K^{-1}$) | Ref. |
|---|---|---|---|---|
| $NaEuF_4$:$Eu^{3+}$ | 298–523 | — | 0.43 | Tian *et al.*[94] |
| $Sr_2GdSbO_6$:$Eu^{3+}$ | 298–423 | 43 | 0.27 | Tai *et al.*[95] |
| $NaLa(MoO_4)_2$:$Eu^{3+}$, $Li^+$ | 303–503 | — | 0.65 | Sonali *et al.*[37] |
| $YVO_4$:$Eu^{3+}$ | 298–473 | 0.39 | 1.08 | Kolensnikov *et al.*[96] |
| $Na_3Y(VO_4)_2$:$Eu^{3+}$ | 298–440 | 1 | 2.4 | Kachau *et al.*[97] |
| $ZnMoO_4$:$Eu^{3+}$,$Li^+$ | 15–295 | 13.9 | 0.61 | Present work |

the populations of the $^7F_0$, $^7F_2$, and $^7F_3$ levels follow a Boltzmann distribution. The overall reduction in photoluminescence intensity at elevated temperatures is primarily due to thermal quenching, confirming thermal extinction as the dominant non-radiative mechanism.

The absolute sensitivity ($S_a$) and relative sensitivity ($S_r$), which quantify the absolute and relative variations in the fluorescence intensity ratio (FIR) with temperature changes, are calculated using the following equations:[92]

$$S_A = \frac{d(FIR)}{dT} = \frac{\Delta E}{kT^2} \times FIR \quad (21)$$

$$S_R = \frac{S_A}{FIR} = \frac{1}{FIR} \times \frac{d(FIR)}{dT} = \frac{\Delta E}{kT^2} \quad (22)$$

Fig. 11(b) and (e) illustrate the dependence of $S_a$ and $S_r$ on temperature for the two FIR ratios 615 nm/579 nm, and 615 nm/653 nm, respectively. The highest sensitivities were observed at 115 K, with $S_a$ values of $13.9 \times 10^{-3}$ $K^{-1}$, and $12.8 \times 10^{-3}$ $K^{-1}$ and $S_r$ values of 0.61% $K^{-1}$, and 0.58% $K^{-1}$ for the 615 nm/579 nm, and 615 nm/653 nm ratios, respectively. Table 3 compares the relative and absolute sensitivity values determined in this study with those reported for other $Eu^{3+}$-doped optical temperature-sensing phosphors, revealing that the sensitivity achieved here is appreciable. Thus, the ZELMO phosphor exhibits promising potential for optical temperature-sensing applications.

The equation below is used to estimate the temperature uncertainty ($\Delta T$):[93]

$$\Delta T = \frac{1}{S_r} \frac{\Delta FIR}{FIR} \quad (23)$$

Here, ΔFIR denotes the standard deviation in the FIR values. Fig. 11c and f illustrate the temperature uncertainty of the ZELMO phosphor corresponding to the intensity ratios $I_{615}/I_{579}$, and $I_{615}/I_{653}$, respectively. The calculated temperature uncertainty is less than 0.76 K, indicating the high precision and reliability of the phosphor for temperature-sensing applications.

### 3.13. Luminescence properties and environmental stability of a flexible phosphor polymer film

The luminescence properties of the ZELMO phosphor matrix embedded in a PVA polymer film are demonstrated through a series of images, providing insights into its emission characteristics, flexibility, and environmental stability. Fig. 12(a) presents the photoluminescence (PL) emission spectra of the film under excitation at 394 nm and 464 nm. The spectra reveal strong luminescence, attributed to the characteristic transitions of $Eu^{3+}$ ions, confirming the efficient incorporation of the phosphor into the polymer matrix. Fig. 12(b) shows the film under both daylight and UV light, with the film demonstrating a distinct pink emission in the UV light. Notably, the film was also folded using forceps in UV light, highlighting its excellent flexibility without a significant loss in luminescent performance. This observation suggests that the phosphor–PVA

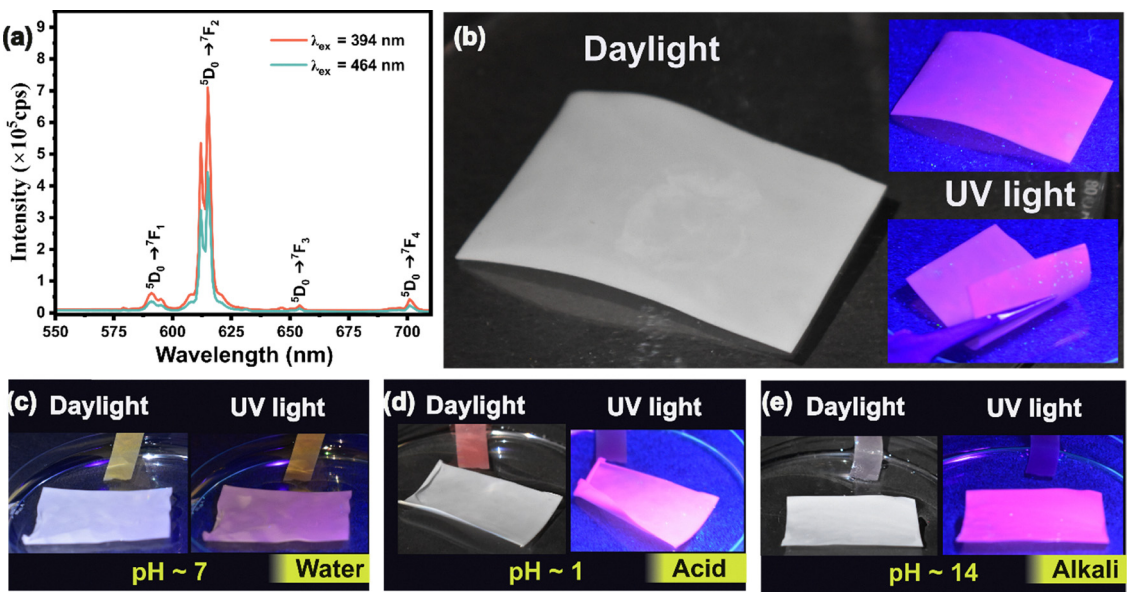


Fig. 12 (a) PL emission spectra of the ZELMO–PVA film at excitation wavelengths of 394 nm and 464 nm. (b) Digital graphics of the ZELMO–PVA film. (c)–(e) Immersion of the phosphor–polymer film in water, acid, and alkali.

composite can be effectively utilized in flexible optoelectronic devices, such as bendable sensors or display technologies.

Fig. 12(c) illustrates the behavior of the film when immersed in a neutral pH 7 aqueous solution, under both daylight and UV light. The film maintains its characteristic pink luminescence in both conditions, indicating the stability of the phosphor under neutral aqueous environments. This property is essential for applications in sensors that may be exposed to aqueous surroundings, suggesting robust chemical stability. Fig. 12(d) and (e) represent the film immersed in an acidic solution (pH 2) and in an alkaline solution (pH 14) respectively, where the pink luminescence is similarly retained. This suggests that the phosphor–PVA film exhibits good resistance to acidic and basic conditions, further broadening its applicability in harsh environments.

## 4. Conclusion

In this study, we systematically investigated $Eu^{3+}$-ion activated $ZnMoO_4$ phosphor materials and optimized the photoluminescent properties for a range of multifunctional applications. By varying the $Eu^{3+}$-ion concentrations and introducing lithium co-doping, we identified the optimal composition, $Zn_{0.88}Eu_{0.09}Li_{0.03}MoO_4$, with enhanced emission intensity and high color purity of 93.6%. The material's suitability as a red component for phosphor-based white LEDs (WLEDs) was established, highlighting its potential in solid-state lighting systems. Furthermore, the material exhibited excellent thermal stability, maintaining 83% of its luminescence intensity at 423 K, underscoring its reliability for diverse lighting applications. It also demonstrated exceptional sensitivity and selectivity for detecting *para*-nitrophenol (4-NP), with a detection range of 1 nM to 200 μM and a detection limit as low as 12 nM, confirming its utility in environmental monitoring and chemical sensing. Additionally, the phosphor showcased reliable performance for low-temperature sensing in the range of 15 K to 295 K, proving its versatility in non-contact optical thermometry. Overall, Li co-doped Eu-doped $ZnMoO_4$ shows significant promise for applications in lighting, sensing, and environmental monitoring, offering a solid foundation for advancing rare-earth-doped phosphor technologies.

## Conflicts of interest

There are no conflicts to declare.

## Abbreviations

| | |
|---|---|
| LED | Light emitting diodes |
| WLED | White light emitting diodes |
| PL | Photoluminescence |
| ZELMO | $Zn_{0.88}Eu_{0.09}Li_{0.03}MoO_4$ |
| 4-NP | *para*-Nitrophenol |

## Data availability

The datasets generated during and analysed during the current study are not publicly available but are available from the corresponding author on reasonable request.

## Acknowledgements

The author, Astha Tyagi, sincerely acknowledges the Council of Scientific and Industrial Research (CSIR) for supporting this research through the CSIR fellowship. The authors, Astha Tyagi and C. Shivakumara, extend their gratitude to the Chemical Science Division at the Indian Institute of Science for providing access to the instrumental facility. They also appreciate the assistance of Ms Nikita Rao (SSCU, IISc) with the NMR experiments and the support of Mr K. Manjunath at the Central Facility, SSCU, IISc, in conducting low-temperature PL experiments. The authors, M. Rakshita and D. Haranath, are grateful to the Council of Scientific and Industrial Research (CSIR) and the Department of Science and Technology (DST), Government of India, for financial support under the projects CSIR-SRF #09/0922(11518)/2021-EMR-I and #CRG/2021/007142, respectively.

## References

1 M. N. Da Silva, J. M. De Carvalho, M. C. De Abreu Fantini, L. A. Chiavacci and C. Bourgaux, *ACS Appl. Nano Mater.*, 2019, **2**, 6918–6927.
2 Y.-H. Han, C.-B. Tian, Q.-H. Li and S.-W. Du, *J. Mater. Chem. C*, 2014, **2**, 8065–8070, DOI: **10.1039/c4tc01336k**.
3 R. S. Yadav, S. J. Dhoble and S. B. Rai, *Sens. Actuators, B*, 2018, **273**, 1425–1434.
4 F. Zhang, H. Zhong, C. Chen, X. G. Wu, X. Hu, H. Huang, J. Han, B. Zou and Y. Dong, *ACS Nano*, 2015, **9**, 4533–4542.
5 J. N. Hao and B. Yan, *Chem. Commun.*, 2015, **51**, 7737–7740.
6 C. Mu, Z. Zhang, Y. Hou, H. Liu, L. Ma, X. Li, S. Ling, G. He and M. Zhang, *Angew. Chem.*, 2021, **133**, 12401–12405.
7 Z. Tang, G. Zhang and Y. Wang, *ACS Photonics*, 2018, **5**, 3801–3813.
8 P. Pust, P. J. Schmidt and W. Schnick, *Nat. Mater.*, 2015, **14**, 454–458.
9 C. Wang, Z. Zhao, Q. Wu, G. Zhu and Y. Wang, *Dalton Trans.*, 2015, **44**, 10321–10329.
10 J. Ling, Y. Zhou, W. Xu, H. Lin, S. Lu, B. Wang and K. Wang, *J. Adv. Ceram.*, 2020, **9**, 45–54.
11 N. C. George, A. J. Pell, G. Dantelle, K. Page, A. Llobet, M. Balasubramanian, G. Pintacuda, B. F. Chmelka and R. Seshadri, *Chem. Mater.*, 2013, **25**, 3979–3995.
12 J. Ueda, P. Dorenbos, A. J. J. Bos, A. Meijerink and S. Tanabe, *J. Phys. Chem. C*, 2015, **119**, 25003–25008.
13 Y. Tian, Y. Wei, Y. Zhao, Z. Quan, G. Li and J. Lin, *J. Mater. Chem. C*, 2016, **4**, 1281–1294.
14 J. Liang, L. Sun, S. Wang, Q. Sun, B. Devakumar and X. Huang, *J. Alloys Compd.*, 2020, **836**, 155469.
15 P. Dang, G. Li, X. Yun, Q. Zhang, D. Liu, H. Lian, M. Shang and J. Lin, *Light: Sci. Appl.*, 2021, **10**, 1–13.

16 C. Ji, H. Zhang, W. Wang, H. Yuan and G. Zhao, *J. Mater. Sci.: Mater. Electron.*, 2023, **34**, 1–10.
17 S. Wang, Y. Xu, T. Chen, W. Jiang, J. Liu, X. Zhang, W. Jiang and L. Wang, *Chem. Eng. J.*, 2021, **404**, 125912.
18 S. Bae, S. Gim, H. Kim and K. Hanna, *Appl. Catal., B*, 2016, **182**, 541–549.
19 W. Yue, M. Chen, Z. Cheng, L. Xie and M. Li, *J. Hazard. Mater.*, 2018, **344**, 431–440.
20 C. Yin, J. Cai, L. Gao, J. Yin and J. Zhou, *J. Hazard. Mater.*, 2016, **305**, 15–20.
21 M. L. Wang, T. T. Jiang, Y. Lu, H. J. Liu and Y. Chen, *J. Mater. Chem. A*, 2013, **1**, 5923–5933.
22 X. Le, Z. Dong, Y. Liu, Z. Jin, T.-D. Huy, M. Le and J. Ma, *J. Mater. Chem. A*, 2014, **2**, 19696–19706.
23 W. Li, H. Zhang, S. Chen, Y. Liu, J. Zhuang and B. Lei, *Biosens. Bioelectron.*, 2016, **86**, 706–713.
24 D. Zhao, D. Yue, L. Zhang, K. Jiang and G. Qian, *Inorg. Chem.*, 2018, **57**, 12596–12602.
25 X. D. Wang, O. S. Wolfbeis and R. J. Meier, *Chem. Soc. Rev.*, 2013, **42**, 7834–7869.
26 A. Shen, S. B. Kim, C. Bailey, A. W. K. Ma and S. Dardona, *IEEE Sens. J.*, 2018, **18**, 9105–9111.
27 A. Wadhwa, J. Benavides-Guerrero, M. Gratuze, M. Bolduc and S. G. Cloutier, *Materials*, 2024, **17**, 2489.
28 M. Mansoor, I. Haneef, S. Akhtar, A. De Luca and F. Udrea, *Sens. Actuators, A*, 2015, **232**, 63–74.
29 Y. Cui, F. Zhu, B. Chen and G. Qian, *Chem. Commun.*, 2015, **51**, 7420–7431.
30 X. Wang, Q. Liu, Y. Bu, C. S. Liu, T. Liu and X. Yan, *RSC Adv.*, 2015, **5**, 86219–86236.
31 Z. Chen, K. Yin Zhang, X. Tong, Y. Liu, C. Hu, S. Liu, Q. Yu, Q. Zhao, W. Huang, Z. Chen, K. Y. Zhang, X. Tong, Y. Liu, C. Hu, S. Liu, Q. Yu, Q. Zhao and W. Huang, *Adv. Funct. Mater.*, 2016, **26**, 4386–4396.
32 M. G. Nikolić, Ž. Antić, S. Ćulubrk, J. M. Nedeljković and M. D. Dramićanin, *Sens. Actuators, B*, 2014, **201**, 46–50.
33 Q. N. Jia, S. Ren, G. W. Yuan and L. Wang, *Appl. Mech. Mater.*, 2013, **343**, 97–100.
34 D. A. Spassky, A. N. Vasil'Ev, I. A. Kamenskikh, V. V. Mikhailin, A. E. Savon, Y. A. Hizhnyi, S. G. Nedilko and P. A. Lykov, *J. Phys.: Condens. Matter*, 2011, **23**, 365501.
35 W. Ran, L. Wang, W. Zhang, F. Li, H. Jiang, W. Li, L. Su, R. Houzong, X. Pan and J. Shi, *J. Mater. Chem. C*, 2015, **3**, 8344–8350.
36 S. C. Abrahams, *J. Chem. Phys.*, 1967, **46**, 2052–2063.
37 Sonali, V. Chauhan, P. C. Pandey and C. Shivakumara, *ACS Appl. Opt. Mater.*, 2024, **2**, 41–56.
38 T. L. Barr and S. Seal, *J. Vac. Sci. Technol., A*, 1995, **13**, 1239–1246.
39 J. R. Rumble, D. M. Bickham and C. J. Powell, *Surf. Interface Anal.*, 1992, **19**, 241–246.
40 D. Aman, S. Abdel-Azim, S. Said and S. G. Mohamed, *RSC Adv.*, 2022, **12**, 7120–7132.
41 Y. Li, H. Li, Y. Li, D. Liu, J. Xie, H. Ma, H. Qu, J. Xu, Y. Han and L. Wang, *Opt. Mater.*, 2023, **144**, 114336.
42 B. V. R. Chowdari, G. V. Subba Rao and C. J. Leo, *Mater. Res. Bull.*, 2001, **36**, 727–736.
43 X. Li, Y. Wang, W. Liu, G. Jiang and C. Zhu, *Mater. Lett.*, 2012, **85**, 25–28.
44 Q. Du, G. Zhou, J. Zhou, X. Jia and H. Zhou, *J. Alloys Compd.*, 2013, **552**, 152–156.
45 B. Zhai, L. Yang and Y. M. Huang, *Nanomaterials*, 2019, **9**, 99.
46 B. Zhai, Q. Ma, L. Yang and Y. M. Huang, *J. Nanomater.*, 2018, **2018**, 1–10.
47 G. R. Dillip and B. Deva Prasad Raju, *J. Alloys Compd.*, 2012, **540**, 67–74.
48 J. Tauc and A. Menth, *J. Non-Cryst. Solids*, 1972, **8–10**, 569–585.
49 J. Tauc, R. Grigorovici and A. Vancu, *Phys. Status Solidi B*, 1966, **15**, 627–637.
50 L. X. Lovisa, Y. L. R. L. Fernandes, L. M. P. Garcia, B. S. Barros, E. Longo, C. A. Paskocimas, M. R. D. Bomio and F. V. Motta, *Opt. Mater.*, 2019, **96**, 109332.
51 W. Zhang, J. Yin, F. Min, L. Jia, D. Zhang, Q. Zhang and J. Xie, *J. Mol. Struct.*, 2017, **1127**, 777–783.
52 S. Jana, A. Mondal, J. Manam and S. Das, *J. Alloys Compd.*, 2020, **821**, 153342.
53 V. Chauhan, P. K. Pandey, P. Dixit, P. Deshmukh, S. Satapathy and P. C. Pandey, *J. Lumin.*, 2022, **248**, 118994.
54 R. Mimouni, A. Souissi, A. Madouri, K. Boubaker and M. Amlouk, *Curr. Appl. Phys.*, 2017, **17**, 1058–1065.
55 D. H. Zhang, Q. P. Wang and Z. Y. Xue, *Appl. Surf. Sci.*, 2003, **207**, 20–25.
56 B. Askri, A. Mhamdi, N. Mahdhi and M. Amlouk, *Phys. B*, 2018, **539**, 51–60.
57 S. K. Gupta, P. S. Ghosh, K. Sudarshan, R. Gupta, P. K. Pujari and R. M. Kadam, *Dalton Trans.*, 2015, **44**, 19097–19110.
58 O. M. Ntwaeaborwa, S. J. Mofokeng, V. Kumar and R. E. Kroon, *Spectrochim. Acta, Part A*, 2017, **182**, 42–49.
59 L. G. Van Uitert, *J. Electrochem. Soc.*, 1967, **114**, 1048.
60 B. Han, J. Zhang, Z. Wang, Y. Liu and H. Shi, *J. Lumin.*, 2014, **149**, 150–154.
61 K. Thomas, D. Alexander, S. Sisira, P. R. Biju, N. V. Unnikrishnan, M. A. Ittyachen and C. Joseph, *J. Mater. Sci.: Mater. Electron.*, 2017, **28**, 17702–17709.
62 S. Saha, S. Das, U. K. Ghorai, N. Mazumder, B. K. Gupta and K. K. Chattopadhyay, *Dalton Trans.*, 2013, **42**, 12965.
63 A. De, B. Samanta, A. K. Dey, N. Chakraborty, T. K. Parya, S. Saha and U. K. Ghorai, *ACS Appl. Nano Mater.*, 2022, **5**, 331–340.
64 S. K. Gupta, K. Sudarshan, A. K. Yadav, R. Gupta, D. Bhattacharyya, S. N. Jha and R. M. Kadam, *Inorg. Chem.*, 2018, **57**, 821–832.
65 E. Sreeja, V. Vidyadharan, S. K. Jose, A. George, C. Joseph, N. V. Unnikrishnan and P. R. Biju, *Opt. Mater.*, 2018, **78**, 52–62.
66 Y. Hua, Sk. K. Hussain and J. S. Yu, *Ceram. Int.*, 2019, **45**, 18604–18613.
67 P. Halappa, B. Devakumar and C. Shivakumara, *New J. Chem.*, 2018, **43**, 63–71.
68 P. Halappa, H. M. Rajashekar and C. Shivakumara, *J. Alloys Compd.*, 2019, **785**, 169–177.

69 C. Shivakumara, R. Saraf, S. Behera, N. Dhananjaya and H. Nagabhushana, *Spectrochim. Acta, Part A*, 2015, **151**, 141–148.
70 S. Som, S. Das, S. Dutta, H. G. Visser, M. K. Pandey, P. Kumar, R. K. Dubey and S. K. Sharma, *RSC Adv.*, 2015, **5**, 70887–70898.
71 R. Saraf, C. Shivakumara, S. Behera, H. Nagabhushana and N. Dhananjaya, *RSC Adv.*, 2015, **5**, 4109–4120.
72 S. C. Lal, A. M. Aiswarya, K. S. Sibi and G. Subodh, *J. Alloys Compd.*, 2019, **788**, 1300–1308.
73 C. Manjunath, M. S. Rudresha, R. H. Krishna, B. M. Nagabhushana, B. M. Walsh, K. R. Nagabhushana and B. S. Panigrahi, *Opt. Mater.*, 2018, **85**, 363–372.
74 M. Fhoula and M. Dammak, *J. Lumin.*, 2020, **223**, 117193.
75 R. Nagaraj, A. Raja and S. Ranjith, *J. Alloys Compd.*, 2020, **827**, 154289.
76 M. A. Patwardhan, R. K. Jumale, R. L. Kohale, R. K. Joshi and S. A. Khapare, *J. Opt.*, 2024, **53**, 4969–4980.
77 M. İlhan, M. K. Ekmekçi and İ. Ç. Keskin, *RSC Adv.*, 2021, **11**, 10451–10462.
78 H. Nalumaga, J. J. Schuyt and G. V. M. Williams, *J. Lumin.*, 2024, **266**, 120251.
79 S. Kalia, R. Kumar, R. Sharma, S. Kumar, D. Singh and R. K. Singh, *J. Phys. Chem. Solids*, 2024, **184**, 111719.
80 F. Liu, F. Liang, Z. Li, G. Kang, T. Wang, C. Chen and Y. Lu, *Analyst*, 2023, **148**, 4030–4036.
81 K.-Y. Hwa, T. S. K. Sharma and A. Ganguly, *Inorg. Chem. Front.*, 2020, **7**, 1981–1994.
82 K. Cao, C. Si, H. Zhang, J. Hu and D. Zheng, *J. Mater. Sci.: Mater. Electron.*, 2022, **33**, 2386–2398.
83 X.-L. Cheng, X. Xia, Q.-Q. Xu, J. Wang, J.-C. Sun, Y. Zhang and S.-S. Li, *Sens. Actuators, B*, 2021, **348**, 130692.
84 J. Shen, L. Liu, W. Huang and K. Wu, *Anal. Chim. Acta*, 2021, **1167**, 338594.
85 W. Zhu, Y. Zhou, S. Liu, M. Luo, J. Du, J. Fan, H. Xiong and H. Peng, *Food Chem.*, 2021, **348**, 129126.
86 S. Hussain, S. De and P. K. Iyer, *ACS Appl. Mater. Interfaces*, 2013, **5**, 2234–2240.
87 A. S. Tanwar, S. Patidar, S. Ahirwar, S. Dehingia and P. K. Iyer, *Analyst*, 2019, **144**, 669–676.
88 J. Sun, J. Zhao, L. Wang, H. Li, F. Yang and X. Yang, *ACS Sens.*, 2018, **3**, 183–190.
89 Y. Wei, L. Cao, L. Lv, G. Li, J. Hao, J. Gao, C. Su, C. C. Lin, H. S. Jang, P. Dang and J. Lin, *Chem. Mater.*, 2018, **30**, 2389–2399.
90 G. Zhang, M. S. Molokeev, Q. Ma, X. Yang, S. Han, Q. Chen, B. Zhong and B. Ma, *CrystEngComm*, 2020, **22**, 5809–5817.
91 Y. Bahrouni, I. Kachou, K. Saidi, T. Kallel, M. Dammak, I. Mediavilla and J. Jiménez, *Mater. Adv.*, 2025, **6**, 1307–1318.
92 Y. Wu, S. Xu, Z. Xiao, F. Lai, J. Huang, J. Fu, X. Ye and W. You, *Mater. Chem. Front.*, 2020, **4**, 1182–1191.
93 I. Kachou, K. Saidi, U. Ekim, M. Dammak, M. Çelikbilek Ersundu and A. E. Ersundu, *Dalton Trans.*, 2024, **53**, 2357–2372.
94 Y. Tian, B. Tian, C. Cui, P. Huang, L. Wang and B. Chen, *Opt. Lett.*, 2014, **39**, 4164.
95 Y. Tai, R. Cui, J. Zhang, C. Wang, T. Zhao, B. Zhang and C. Deng, *J. Rare Earths*, 2024, **42**, 1458–1469.
96 I. E. Kolesnikov, A. A. Kalinichev, M. A. Kurochkin, D. V. Mamonova, E. Y. Kolesnikov and E. Lähderanta, *J. Phys. Chem. C*, 2019, **123**, 5136–5143.
97 I. Kachou, K. Saidi, R. Salhi and M. Dammak, *RSC Adv.*, 2022, **12**, 7529–7539.